Biasing relation, environmental dependencies and estimation of the growth rate from star forming galaxies

Adi Nusser,[1] Gustavo Yepes,[2, 3] and Enzo Branchini[4, 5, 6]

[1]*Department of Physics and the Asher Space Research Institute, Israel Institute of Technology Technion, Haifa 32000, Israel*

[2]*Departamento de Física Teórica M-8, Universidad Autónoma de Madrid, Cantoblanco, E-28049 Madrid, Spain*

[3]*Centro de Investigación Avanzada en Física Fundamental (CIAFF), Facultad de Ciencias, Universidad Autónoma de Madrid, E-28049 Madrid, Spain*

[4]*Dipartimento di Fisica, Università di Roma, 3, via della Vasca Navale 84, I-00146 Roma, Italy*

[5]*INFN - Sezione di Roma Tre, via della Vasca Navale 84, I-00146 Roma, Italy*

[6]*INAF - Osservatorio Astronomico di Roma, via Frascati 33, I-00040 Monte Porzio Catone (RM), Italy*

ABSTRACT

The connection between galaxy star formation rate (SFR) and dark matter (DM) is of paramount importance for the extraction of cosmological information from next generation spectroscopic surveys that will target emission line star forming galaxies. Using publicly available mock galaxy catalogs obtained from various semi-analytic models (SAMs) we explore the SFR-DM connection in relation to the *speed-from-light* method (Feix et al. 2017) for inferring the growth rate, f, from luminosity/SFR shifts. Emphasis is given to the dependence of the SFR distribution on the environment density on scales of 10s-100s Mpc. We show that the application of the *speed-from-light* method to an Euclid-like survey is not biased by environmental effects. In all models, the precision on the measured $\beta = f/b$ parameter is $\sigma_\beta \lesssim 0.17$ at $z = 1$. This translates into errors of $\sigma_f \sim 0.22$ and $\sigma_{(f\sigma_8)} \sim 0.1$, without invoking assumptions on the mass power spectrum. These errors are in the same ballpark as recent analyses of the redshift space distortions in galaxy clustering. In agreement with previous studies, the bias factor, b is roughly a scale-independent, constant function of the SFR for star forming galaxies. Its value at $z = 1$ ranges from 1.2 to 1.5 depending on the SAM recipe. Although in all SAMs denser environments host galaxies with higher stellar masses, the dependence of the SFR on the environment is more involved. In most models the SFR probability distribution is skewed to larger values in denser regions. One model exhibits an *inverted* trend where high SFR is suppressed in dense environment.

Keywords: galaxies: halos - cosmology: theory, dark matter, galaxies

1. INTRODUCTION

The connection between the dark matter and galaxies is essential for understanding the processes that regulate the formation and the evolution of galaxies and, consequently, to derive cosmological parameters from the analysis of galaxy redshift surveys. In particular, estimation of cosmological parameters from the clustering pattern is inherently dependent on this connection.

In the standard paradigm galaxies form by the condensation and cooling of gas inside DM dominated halos (virialized objects) (Binney 1977; Rees & Ostriker 1977; Silk 1977; White & Rees 1978). The process is hierarchical (Peebles 1980) with early forming galaxies collapse into and merge with other galaxies and is greatly affected by energy re-

leased from supernovae (Larson 1974; Dekel & Silk 1986) and AGN activities (Silk & Rees 1998).

Semi-analytic galaxy formation models (SAMs) (White & Frenk 1991; Kauffmann et al. 1993; Lacey et al. 1993; Somerville & Primack 1999) have been extensively employed in an attempt to understand the vast amount of observational properties of galaxies and the link to the formation of supermassive blackholes. SAMs approximates complex interconnected processes of star formation, energetic feedback and hydrodynamics in terms of simple forms involving a large number of free parameters. The importance of each process can then by assessed by tuning the relevant parameters to match certain observational data.

State-of-the-art cosmological simulations can now follow the hydrodynamics in conjunction with elaborate (albeit poorly known) sub-grid physics of galaxy formation over large dynamical scales (Gene et al. 2014; Khandai et al. 2015; Schaye et al. 2015; Dolag et al. 2016; Dubois et al. 2016). Unfortunately, the box size of this type of simu-

adi@physics.technion.ac.il

lations remains insufficient to describe the structure on the large scales probed by large redshift surveys. As an example, Illustris TNG300 (Springel et al. 2018) has a box size of 205 h^{-1} Mpc on a side, equivalent to only 25% the volume probed by the low redshift Two Mass Redshift Survey (2MRS, Huchra et al. 2012) and substantially smaller than the volume coverage planned by future large surveys.

DM-only simulations on the other hand have been done for large simulation boxes of several Gpcs. Kauffmann et al. (1997) pioneered the approach of incorporating SAMs in DM only simulations. The simulation used in that work was only of a box size of 128 Mpc. The same approach was later applied by many workers in the field using much larger simulations and more elaborate SAMs (e.g. Kauffmann et al. 1999; Benson et al. 2000; Guo et al. 2011; Angulo et al. 2014; Baugh et al. 2019).

Numerical and semi-analytic methods have been extensively used to study the *biasing* relation between the distribution of galaxies and the underlying distribution of mass (DM-dominated) as a function of the stellar mass. fHowever, next-generation spectroscopic galaxy redshift surveys like the Dark Energy Spectroscopic Instrument (DESI) survey (DESI Collaboration et al. 2016), the Euclid space mission (Euclid Collaboration et al. 2019) and the Roman space mission (Akeson et al. 2019) will mainly select objects based on SFR indicators like the Hα and the [OII] emission lines. Therefore the biasing relation for galaxies selected based on star formation rates is becoming of particular interest (Angulo et al. 2014).

In general, the biasing relation enters in any analysis based on the clustering of galaxies. Its knowledge is essential for a precise and accurate estimation of cosmological parameters. It is at the heart of methods relying on the anisotropy of clustering in redshift space (the so-called redshift space distortions, hereafter RSDs) (Sargent & Turner 1977) and, to a lesser degree, in analysing signatures of Baryonic Acoustic Oscillations (BAO). The standard and most convenient assumption is that of *linear biasing*. If $1 + \delta_{\mathrm{gal}}$ and $1 + \delta$ are the galaxy number density and the total mass density in units of their respective mean values, linear biasing dictates

$$\delta_{\mathrm{gal}}(t, \mathbf{r}) = b(t)\delta(t, \mathbf{r}) + \varepsilon \,, \tag{1}$$

where b is independent of δ and position $\mathbf{r}$, but is a function of time as implied by continuity considerations (Nusser & Davis 1994; Tegmark, M. Peebles 1998). The term ε represents stochastic (random) scatter around the mean relation (e.g. Dekel & Lahav 1999). Both density contrasts, δ_{gal} and δ, are assumed to have been filtered with the same smoothing window. For gaussian random fields, the relation is valid on sufficiently large scales (Bardeen et al. 1986). The term ε arises from an intrinsic scatter in the biasing relation as well as the Poisson fluctuations (shot noise) associated with

the finite number of galaxies. The intrinsic scatter can be attributed to several factors that are not captured solely by the local mass density field at a given time. The assembly and star formation history, details of the feedback process and external gravitational tidal field that affects the galaxy rotation, all can impact the galaxy properties. Linear biasing has been demonstrated to hold on sufficiently large scales and its dependence on the stellar mass and the host halo mass has been studied using simulations as well as analytic models.

Modern spectroscopic redshift surveys are designed to provide tight constraints on the growth rate, f, of linear density fluctuations at high redshift. The growth rate is related to the growing density mode D via (Peebles 1980)

$$f = \frac{\mathrm{dln}\, D}{\mathrm{dln}\, a} \approx \Omega^{\gamma} \tag{2}$$

with $\gamma \approx 0.55 + 0.05(1 + w)$ for a dark energy model with an equation of state parameter w (Linder 2005). Therefore, constraining f at different cosmic epochs could in principle yield important insight into the dark energy models responsible for the accelerating expansion of the Universe. The aforementioned RSDs resulting from placing galaxies at their redshifts rather than actual distances are a traditional probe of f via the combination

$$\beta \equiv \frac{f(\Omega)}{b} \,. \tag{3}$$

But, placing galaxies at their redshift positions rather than actual distances, does not only result in RSDs. It also shifts the estimates of the galaxy intrinsic luminosities from their true values obtained using actual distances. To first order, the redshift position differs from the distance by the line of sight (los) peculiar velocity. Therefore, coherent large scale luminosity variations in space, can be used to constrain the peculiar velocity field. This idea dates back to the work of Tammann et al. (1979) who correlated the magnitudes of nearby galaxies with their redshifts to constrain the velocity of the Virgo cluster relative to the Local Group.

There are two techniques to probe the velocity field using luminosity variations. In the first one, direct constraints on the velocity are derived using the observed variations. This technique has been applied to the 2MRS at $z \lesssim 0.03$ (Nusser et al. 2011; Abate & Feldman 2012; Branchini et al. 2012) and the Digital Sloan Sky Survey (SDSS) at $z \sim 0.1$ by Feix et al. (2015, 2017), and led to interesting constraints on the amplitude of the bulk flow. This technique is susceptible to environmental dependence of the luminosity distribution. Indeed, the dependence of the luminosity function on the large scale density field could mimic variations due to peculiar velocities. For nearby surveys like the 2MRS, the luminosity shift from peculiar velocities dominates over environmental effects. However, at $z \approx 1$, relevant to next generation surveys this is not the case anymore, making the application of

this technique less attractive or even irrelevant in comparison to low redshift surveys.

The second technique relies on a simultaneous estimation of the luminosity fluctuation and the peculiar velocity field from the actual galaxy distribution in redshift space (Nusser et al. 2012). The derived velocity field depends on β. The true galaxy luminosities are then estimated using the distances derived from the redshifts by subtracting the los peculiar velocities. The parameter β is derived by minimizing the large scale spatial luminosity variations. Assuming the environmental dependence of the luminosity function are mostly via the large scale density, this method will yield an unbiased estimate of β thanks to the lack of correlation between the density and the peculiar velocity at a given point in space. In general, Galilean invariance can be invoked to conclude that the peculiar motion of a galaxy cannot affect any of its internal properties. Therefore, any mechanism that affects the luminosity distribution to a given point in space must be uncorrelated with the peculiar velocity at the same point. Thus environmental dependencies will only affect the statistical uncertainty in the derived estimates of β. We gave the name Speed-from-Light (hereafter, SFLM) (Feix et al. 2017) to this second method.

The third goal of this paper is to provide an assessment of the applicability of this method for constraining β from next generation spectroscopic redshift survey and to verify its sensitivity to environmental effects. We wish to confirm that environmental dependencies do not bias the β estimate from the SFLM and to estimate how they affect the random error assigned to β.

We will rely on mock galaxy catalogs obtained by applying different SAM recipes to large DM-only simulations. Mock catalogs are likely inaccurate at describing galaxy properties at high redshift. We therefore compare predictions from different models to achieve different goals. First, we aim at identifying common features that can be used as a predictions for planned surveys. Second, the discrepancies among the models will serve to appreciate the scatter in current theoretical predictions. And third we will assess how environmental dependencies, which can be quantified in future observations, can provide useful constraints on models of galaxy formation

The outline of the paper is as follows. In §2, we present the simulations and the corresponding mock galaxy catalogs that we use in this work and their relation to next generations spectroscopic catalogs. In §3 we use mock catalogs to study how stellar masses and star formation rate depend on the environment. In §4 we focus on galaxy biasing and its dependence on the SFR and stellar mass. The impact of the large scale environment on the estimate of β from the SFLM method is studied in §5. We discuss our results and offer our conclusions in Sections 6 and 7, respectively.

Table 1. Relevant parameters of the three MDPL simulations used in this work. All simulations correspond to a ΛCDM cosmology with parameters $h = 0.6777$, $\Omega_\Lambda = 0.692885$, $\Omega_{\rm m} = 0.307115$ and $\sigma_8 = 0.8228$

	SMDPL	MDPL2	BigMDPL
$L\,[\,{\rm h}^{-1}\,{\rm Mpc}]$	400	1000	2500
$m_p\,[10^8 M_\odot]$	1.42	22.3	348

2. MOCKS AND SIMULATIONS

We use publicly available mock galaxy catalogs extracted from three DM-only simulations (SMDPL, MDPL2, BigMDPL) of the MULTIDARK suites. The relevant parameters of the simulations are listed in Table 1. Mock galaxy catalogs from the SAG (Cora et al. 2018) , SAGE (Croton et al. 2016) and GALACTICUS (Benson 2012) semi-analytic galaxy formation models (SAMs), are publicly available only for the MDPL2 simulation. These mocks, referred to as MULTIDARK-GALAXIES (Knebe et al. 2018) have been downloaded from the COSMOSIM data base[1]. Mock galaxies extracted from the SMDPL simulation are available only for the UNIVERSEMACHINE (hereafter UM, Behroozi et al. 2019) a self-consistent empirical galaxy formation model and have been kindly provided by Peter Behroozi. The UM model offers a simple recipe for assigning SFR to halos. We use that recipe to populate the MDPL2 and BigMDPL simulations with galaxies based on the UM mocks in the SMDPL.

All SAMs incorporate the same basic processes of galaxy formation, gas cooling, star formation according to the amount of cold gas, stellar winds and AGN feedback. They include recipes for tracing the mass in the main galaxy components: disks, bulges, black holes. The models have a large number of free parameters that are fixed by matching observations of the galaxy population. Despite their similarities, the three SAMs differ in the way baryonic physical processes are implemented. For example, all of them basically follow the gas cooling treatment presented in White & Frenk (1991), but differ in the details of metal cooling. GALACTICUS follows the SFR recipe in Krumholz et al. (2009), while SAG initiates star formation only once the cold gas mass in the forming disk exceeds a certain value. In addition to the radio mode AGN feedback employed in SAG and GALACTICUS, SAGE also includes a quasar wind mode. Another difference between SAGE and the two other models is the treatment of galaxies which no longer have identifiable parent subhalos in the simulation. SAGE disperses the stellar content of orphan galaxies into the main halo, while GALACTICUS and SAG maintain them as separate entities, However, since we

---

[1] https://www.cosmosim.org

will focus on galaxies with high SFR, we do not expect our results to depend on this aspect of the models.

Comparison between SAG, SAGE and GALACTICUS applied to MDPL2 is provided in Knebe et al. (2018). All models have been calibrated using low redshift, $z \approx 0$, key observational data such as the black hole - bulge mass relation and the stellar mass functions, but not always to the same data compilation (c.f. Table 1 in Knebe et al. 2018).

We are mostly interested in results at $z = 1$ to match the typical redshift of next generation surveys. Therefore we shall focus on $z = 1$ simulated catalogs and only consider the $z = 0$ case to explore the biasing of star forming galaxies at lower redshift.

2.1. UNIVERSEMACHINE *Mock galaxies for MDPL2 and BigMDPL*

The UM models available for us are only for the SMDPL simulation of insufficient volume to probe the dependence of the SFR and luminosity distributions on the galaxy environment. Therefore, we wish to generate UM mock galaxies for the larger boxes as well. The main usage for UM in these larger boxes will be to estimate the cosmic variance. Fortunately, in the UM models, the SFR in a halo at redshift z depends mainly on V_{M_p}, the maximum of the rotation curve measured at the peak mass through the history of the halo until z (Behroozi et al. 2019). This is not necessarily true for satellite galaxies that do not play a significant role in our analysis since we are interested in large star forming galaxies. Also, since we are mainly interested in the SFR rather than stellar mass, we avoid running the whole UM machinery by assigning SFRs to MDPL2 and BigMDPL halos from a random re-sampling of the SFR conditional probability distribution given V_{M_p}, taken from the full UM in the SMDPL simulation [2]. Instead, for each halo in the larger simulations, we select a value for SFR from the distribution in the $V_{M_p} - $ SFR in SMDPL. The re-sampling will capture environmental dependencies present in the distribution of V_{M_p}, but will miss those associated with other parameters that can have an effect on the SFR. Nonetheless, these re-sampled catalogs will mainly serve for the statistical assessments of the SFLM. An added value for random re-sampling is that several realisations of SFRs can be generated for the same halo. This allows an assessment of randomness (stochasticity) in the SFR per halo assignment, at least in the UM models.

The top panel in Fig. 1 shows the distribution of a randomly selected fraction of mock galaxies in the SFR $- V_{M_p}$ plane from the full UM model in SMDPL. Also plotted are contours of the two dimensional (2D) probability distribution function (PDF) of $\log$ SFR and $\log V_{M_p}$. The two branches of

star forming and quenched (low star formation) galaxy population are clearly visible. As we shall see in the next Section, next generation surveys like Euclid will observe galaxies with relatively high SFR > 10 M$_\odot$ yr^{-1}, sampling the tip of the PDF.

The middle and bottom panels show, respectively, the same distributions for MDPL2 and BigMDPL obtained by re-sampling SFR at a given V_{M_p} from the distribution represented in the top panel. In practice, we partition the SMDPL galaxies in 100 bins in $\log V_{M_p}$ and match the bins to V_{M_p} of halos in the larger simulations. Then the distribution of UM SFR values in each bin is randomly sampled to assign SFR values to the respective halos in the larger simulations. Due to the larger particle mass in the larger simulations, they do not resolve low V_{M_p} as the SMDPL does, yielding lower number densities of galaxies relative to the SMDPL. Table 2 lists the number densities of UM galaxies in SMDPL and in the re-sampled UM in the two larger simulations, which we label UM MDPL and UM BigMDPL. This table refers to redshift $z = 1$ and two different M_* cuts, as indicated. We emphasize that the re-sampling does not provide M_* for the larger simulations, only SFR. The number densities in SMDPL and MDPL2 are comparable, with the latter having only a 11% lower value, while UM BigMDPL is significantly more dilute. Still, the number densities of all models in the Table are consistent with each other within a factor of two. In addition, the BigMDPL box represents a sizable fraction of the volume that will be probed by the Euclid's spectroscopic survey and contains a comparable total number of galaxies (Euclid Collaboration et al. 2019).

An important check of the re-sampling procedure is whether it yields consistent clustering properties among the three UM catalogs. In Fig. 2 we plot the quantity $\Delta(k) \propto k^3 P_{gal}(k)$ where $P_{gal}(k)$ is the galaxy power spectrum as a function of the wave number k. The details of computing P_{gal} are described in §4. The figure indeed demonstrates a very good agreement between the three power spectra.

2.2. *Volumes and Galaxy Densities: connection to observations*

The results of the present study are relevant for any spectroscopic surveys that, like DESI, Euclid and Roman-WFIRST, will target emission line galaxies over large sky areas at intermediate redshifts. Here we will focus on the Euclid case and consider it as representative of a typical next generation spectroscopic surveys.

Euclid's survey will detect Hα galaxies with line flux larger than 2×10^{-16} erg s^{-1} cm^{-2}, over 15000 deg^2 of the sky in the redshift range $0.9 < z < 1.8$ corresponding to comoving volume of ~ 43 h^3 Gpc^{-3}. Based on models calibrated on available observations of Hα emitters (Pozzetti et al. 2016), the Euclid collaboration has recently provided

---

[2] The quantity V_{M_p} is available from the Rockstar catalogues for all halos in all simulations.
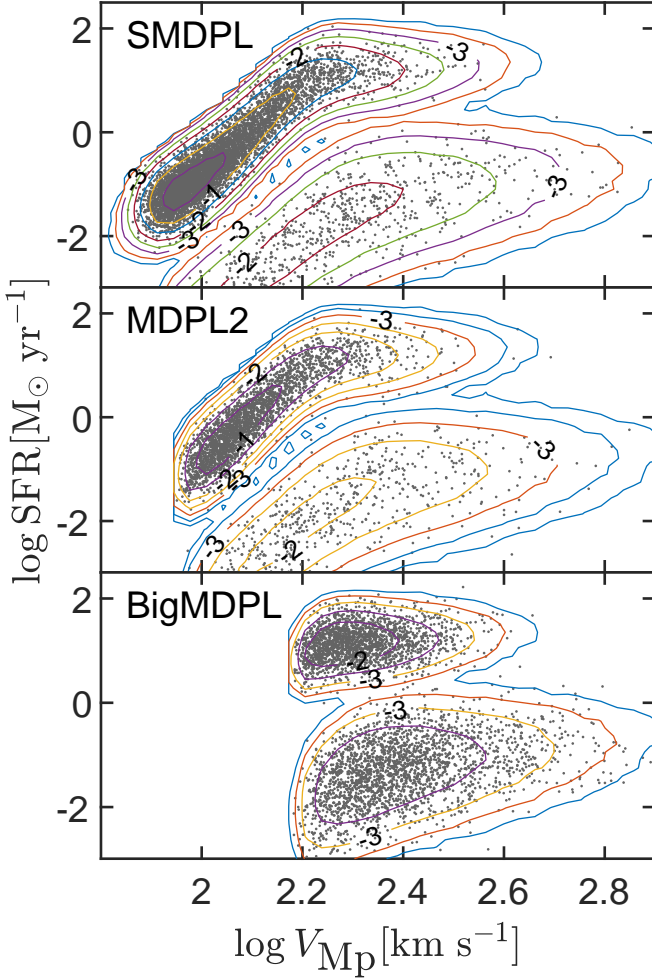
Figure 1. The distribution of UM galaxies in the plane $\log \mathrm{SFR}$ and $\log V_{\mathrm{M_p}}$. Top: galaxies in the UM catalog extracted from the SMDPL simulation. In middle (MDPL2) and bottom (Big-MDPL), SFRs were assigned to halos with a given $V_{\mathrm{M_p}}$ by re-sampling of the distribution in the top panel. Contours designate certain values of the logarithm of 2D probability distribution function $P(\log \mathrm{SFR}, \log V_{\mathrm{M_p}})$.

their forecast for the number density of Hα galaxies: one expects $n \sim 6.9 \times 10^{-4} h^3 \, \mathrm{Mpc}^{-3}$ at $z \sim 1$, gradually decreasing to $n \sim 4.2 \times 10^{-4} h^3 \, \mathrm{Mpc}^{-3}$ at $z \sim 1.4$ and dropping to $n \sim 2.6 \times 10^{-4} h^3 \, \mathrm{Mpc}^{-3}$ at $z \sim 1.7$.

Galaxy formation models provide the SFR rather than the luminosity, $L_{H\alpha}$, of the Hα line. To link these quantities we adopt the transformation (e.g. Domínguez Sánchez et al. 2012)

$$\log \mathrm{SFR}[\mathrm{M_\odot \ yr^{-1}}] = \log L_{H\alpha}[\mathrm{erg \ s^{-1}}] - 41.1 \ . \quad (4)$$

The Euclid Hα flux cut corresponds then to a lower SFR threshold $\mathrm{SFR_{lim}} = 10 \ \mathrm{M_\odot \ yr^{-1}}$ at $z = 1$. For mock galaxies with $M_* > 5 \times 10^9 \mathrm{M_\odot}$, the number densities, listed in Table 2 are higher than the official Euclid fore-
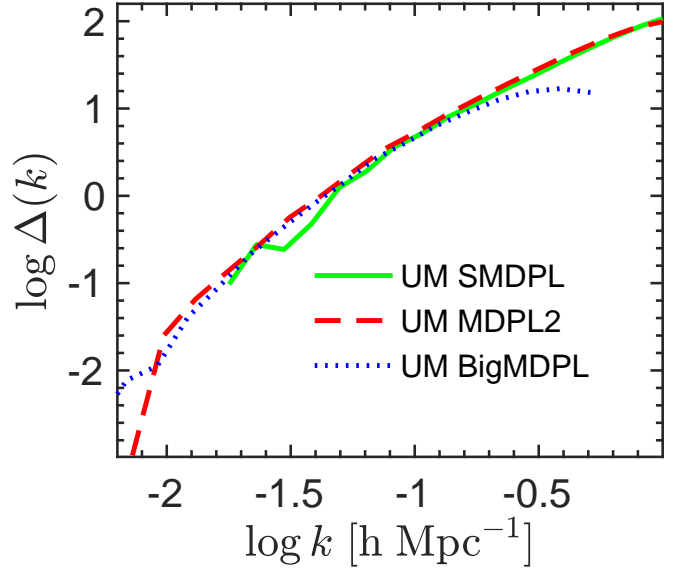

Figure 2. Consistency of power spectra of the mock galaxies in the the full UM in SMDPL and in the UM MDPL and UM BigMDPL samples.

cast. However, they are comparable to those of Model 1 of Pozzetti et al. (2016) since they expect a number density of $2.6 \times 10^{-3} h^3 \mathrm{Mpc}^{-3}$ galaxies above the Euclid Hα flux threshold. This is actually close to the number densities of galaxies with $\mathrm{SFR} > 10 \ \mathrm{M_\odot \ yr^{-1}}$ and $M_* > 5 \times 10^8 \mathrm{M_\odot}$ in the mock catalogs, as seen in Table 2. This is perhaps not surprising since the Euclid forecast account for instrumental effects and observational biases that are not included in the simulations.

The MDPL2 box is $\sim 2.3\%$ the total volume probed by the full Euclid survey and $\sim 12\%$ the volume in the redshift bin $[0.9 - 1.1]$. In this redshift range the Euclid Collaboration et al. (2019) expects to observe more than (10^6) galaxies, i.e. roughly the number of objects required for a successful application of the SFLM method. The mocks, however, approximately contain this number of galaxies in the MDPL2 volume alone. Therefore, it is fortunate that the number density in the simulations is higher that the expectations of (Euclid Collaboration et al. 2019), as this will allow us to test the SFLM already with the mocks we have. The shortcoming is that the smaller simulated volume prevents a proper assessment of cosmic variance.

The larger simulation BigMDPL is $\sim 36\%$ of the full spectroscopic survey, still small to perform cosmic variance estimation. However, it is helpful in constraining cosmic variance on smaller scales, which can point towards its magnitude for the whole Euclid survey.

Table 2. Number of galaxies with SFR $> 10\ \mathrm{M}_\odot\ \mathrm{yr}^{-1}$ in the mock catalogs at $z = 1$. Top two entries list the total number of galaxies in the simulation boxes for two different stellar mass thresholds. The bottom two entries list the galaxy number densities $n = N_{\mathrm{gal}}/L^3$ in the same boxes.

Mock catalog	SAG	SAGE	Galac	UM	UM MDPL2	UM BigMDPL
Simulation	MDPL2	MDPL2	MDPL2	SMDPL	MDPL2	BigMDPL
$N_{\mathrm{gal}}, M_* > 5 \times 10^9 \mathrm{M}_\odot$	3.29×10^6	4.48×10^6	2.07×10^6	3×10^5	4.15×10^6	3.4×10^7
$N_{\mathrm{gal}}, M_* > 5 \times 10^{10} \mathrm{M}_\odot$	7.43×10^5	1.73×10^6	9.5×10^4	5.88×10^4	–	–
$n\ [\mathrm{h}^3\mathrm{Mpc}^{-3}], M_* > 5 \times 10^9 \mathrm{M}_\odot$	3.29×10^{-3}	4.48×10^{-3}	2.07×10^{-3}	4.67×10^{-3}	4.15×10^{-3}	2.20×10^{-3}
$n\ [\mathrm{h}^3\mathrm{Mpc}^{-3}], M_* > 5 \times 10^{10} \mathrm{M}_\odot$	7.43×10^{-4}	1.73×10^{-3}	9.5×10^{-5}	9.12×10^{-4}	–	–

3. STELLAR MASS AND STAR FORMATION RATE

Properties of the MULTIDARK-GALAXIES have been studied extensively by Knebe et al. (2018). Nonetheless, for completeness and as a basic check on our analysis, we compute the stellar mass and SFR distribution functions from the downloaded data and compare our results with Knebe et al. (2018) whenever relevant. For this validation test we will consider two epoch, $z = 0$ and $z = 1$.

In Figs. 3 & 4, we plot the distribution of a randomly selected fraction of galaxies in the plane $\log \mathrm{SFR} - \log M_*$ at $z = 1$ and $z = 0$, respectively. Instead of the SFR, Knebe et al. (2018) plot the specific SFR defined as the SFR per unit stellar mass. Since we are interested in galaxies selected according to the SFR, it is more instructive for our purposes to explore the distribution $\mathrm{SFR} - M_*$ plane. A bimodal structure is recognizable at both redshifts for the UM (SMDPL) galaxies. This is not surprising since these models impose a division into a quenched and active galaxies. At $z = 1$, all models except GALACTICUS produce a tight "main sequence" of star forming galaxies with similar slope and normalization, although it is broader in the SFR direction for SAGE as can be seen from the plotted contours. A main sequence can be identified in GALACTICUS at $z = 0$, as the point encompassed by purple contours, but the overall distribution is much more diffuse than the other models. This figure demonstrates the complexity of the relation between the SFR and stellar mass. The large scatter and the shape of the distribution make it hard to associate a well-defined stellar mass to a given SFR.

The left and right panels of Fig. 5 show the 1D distribution functions for SFR and the stellar mass, respectively. Apart from the MULTIDARK-GALAXIES mocks, the figure also shows results from the UM (SMDPL) simulation. Models generally agree with the measured PDF of the SFR except for SAGE that under-predicts the counts in the high-SFR tail. The stellar mass functions at $z = 0$ (right bottom panel) for SAG, SAGE and GALACTICUS are in agreement with the corresponding curves at $z = 0.1$ in figure 1 of Knebe et al. (2018). All curves in each panel are roughly in the same ballpark, but the deviations are significant even at $z = 0$. This
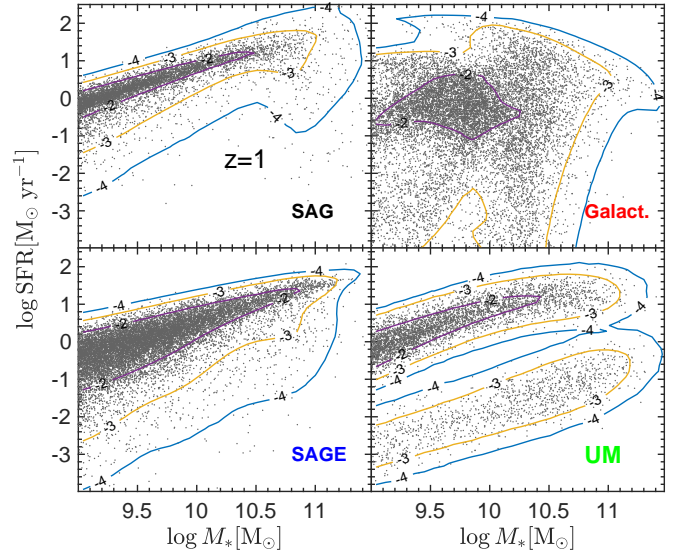

Figure 3. The distribution of galaxies in the $M_* - \mathrm{SFR}$ plane at $z = 1$ in different mock catalogs. Contours designate certain values of the 2D PDF of $\log \mathrm{SFR}$ and $\log M_*$.

is not surprising due to the differences in the modelling and calibration to observations. As pointed out by Knebe et al. (2018), SAGE produces the best match to the observed stellar mass distribution at $z = 0$ as reported by Moustakas et al. (2013) (bottom right). Also, since Moustakas et al. (2013) found little evolution of the observed stellar mass distribution since $z = 1$ we can take observations at $z = 0$ as representative to those at at $z \approx 1$ and see that only SAG over-produces galaxies at the high mass end. At $z = 0$, both SAG and GALACTICUS curve are above the observations at the high mass end. Knebe et al. (2018) attribute this $z \approx 0$ excess to less efficient AGN suppression of star formation compared SAGE.

3.1. Environmental dependencies

The large scale environment can play a role in shaping the properties of galaxies (e.g. Xu et al. 2020). Minor differences in assembly history of halos of the same mass (e.g Gottlober et al. 2001; Sheth & Tormen 2002; Gao & White 2007) can
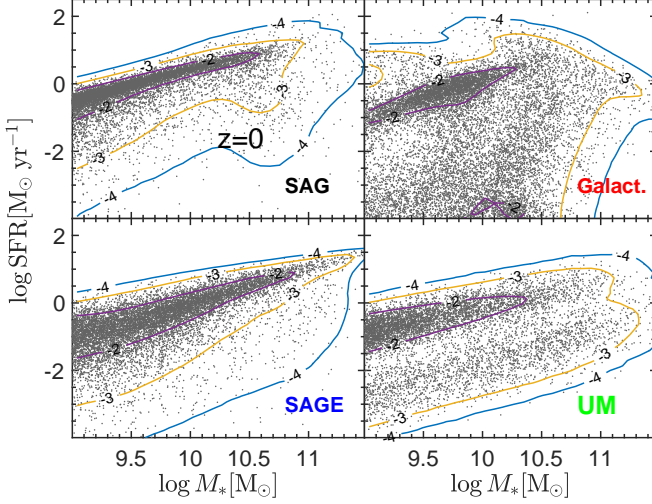
**Figure 4.** Same as the previous figure, but for $z = 0$.
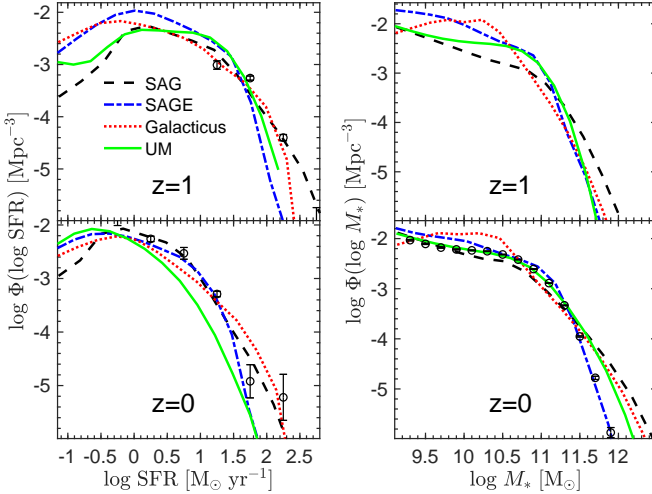
Figure 5. The number density of SAM galaxies as a function of the SFR (panels to the left) and the stellar mass (to the right right) for redshift $z = 0$ (bottom) and $z = 1$ (top). Different model predictions are represented by curves with different linestyles, specified in the labels. The open circles are data with errorbars from Gruppioni et al. (2015) (left) and Moustakas et al. (2013) (right).

lead to significant differences in their SFR evolution and the final stellar mass. Here we are interested in the modulation of the SFR and stellar mass distributions, as a function of the large scale density smoothed on scales of tens to hundreds of Mpc.

In all mocks, the mass density of the DM is provided on a cubic grid. We use Fast Fourier Transform (FFT) to smooth the mass density with a Top-Hat (TH) window of width $R_s = 20$ and 100 h^{-1} Mpc, respectively. Densities,

δ_i, at the galaxy positions are obtained by linear interpolation of the smoothed density fields on the grid.

We compare SFRs and M_*-values in low vs. high density environment by comparing the PDFs of $\log$ SFR and $\log M_*$ estimated for galaxies with the lowest versus highest 20% values of δ_i.

The PDF of $\log$ SFR is computed for galaxies with SFR > 10 $M_\odot$ yr^{-1} to match the cut of the Euclid survey and $M_* > 5 \times 10^9$ $M_\odot$. Conversely, no cut in $\log$ SFR is imposed in the the PDF of $\log M_*$. The results are plotted in Fig. 6 and Fig. 7, referring to two different environment scales of $R_s = 20$ and 100 h^{-1} Mpc, respectively. In all models there is a clear dependence on the environment density, which is more pronounced at the high end of either $\log$ SFR or $\log M_*$. A reduction in the abundance of high M_* galaxies in low density environments, is evident in the panels to the right, where at high M_* the dashed curve (low δ_i) is below the solid (high δ_i) for all models.

The SFR relation to the environment is more involved. Except GALACTICUS, high density environments are associated with higher SFRs. GALACTICUS exhibits an intriguing "inverted dependence" on δ_i; the PDF is skewed toward higher SFR for galaxies in a low rather than high density environment. This implies a relatively more active star formation in galaxies in low than high density environments . We can compromise this behavior in GALACTICUS with the trend of increased fraction of high M_* at high densities, if the star formation in dense regions is preferentially intensified well earlier than $z = 1$.

The curves are closer to each other for the larger $R_s = 100$ h^{-1} Mpc smoothing. The reason for that is mainly the narrower density range in the larger smoothing. Note the density ranking is not preserved between the two smoothed density fields, otherwise the two figures would be identical.

It is also interesting to examine the mean $\log$ SFR at a given $\log M_*$ versus density. This is plotted in Fig. 8 where the red dashed and blue solid lines, respectively, correspond to galaxies with lowest 20% and highest 20% densities. For this plot only, the density is smoothed on a scale $R_s = 8$ h^{-1} Mpc. The error bars represent the rms of the scatter of individual galaxies around the mean curves. The red curves do not reach as high M_* as the blue, simply because of the reduction of galaxies with this high M_* in low density environments. The UM and SAGE galaxies exhibit very little dependence on the density of the environment. SAG galaxies follow similar curves in low and dense environments for $\log M_* \lesssim 11$ at both redshifts, even for this small $R_s = 8$ h^{-1} Mpc. For GALACTICUS, the only signature of the environment is a boost in the SFR in low densities for $\log M_* \lesssim 10$.

### 3.1.1. *Parametrisation of Environmental Dependencies*
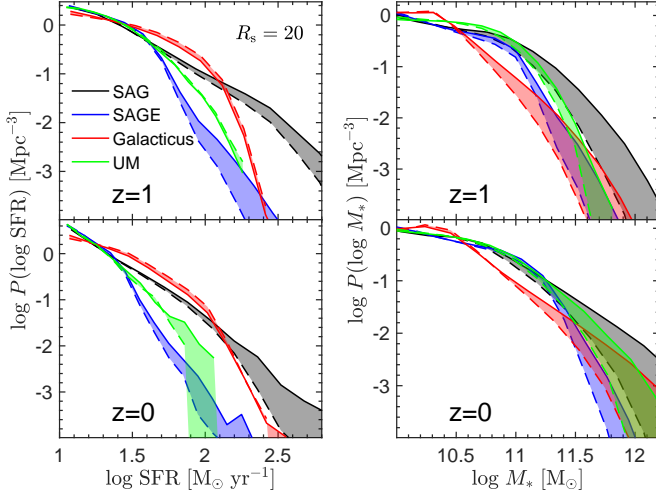
Figure 6. The PDF of $\log \mathrm{SFR}$ (left) and $\log M_*$ (right) as a function of the DM density smoothed with a TH window of width $R_s = 20$ h^{-1} Mpc, at $z = 1$ (top) and $z = 0$ (bottom). Dashed and solid curves correspond to least and most 20% dense regions. The area between these curves for each SAM is color marked, as indicated in the figure. The figure refers to galaxies satisfying our Euclid cut of SFR mass greater than 10 $M_\odot$ yr^{-1} and stellar mass $5 \times 10^9 M_\odot$, respectively.
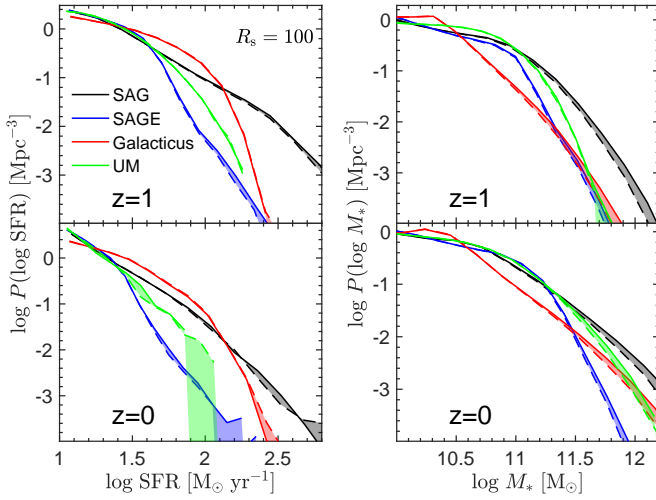
Figure 7. Same as Fig 6, but for $R_s = 100$ h^{-1} Mpc.

We focus here on the SFR as it is relevant for the SᴛLM applied to emission line surveys. We parameterize the dependence of the SFR on the smoothed mass density, δ, as

$$\log \mathrm{SFR}_i = c_1 + c_2 \delta_i + \mathcal{R}_i , \qquad (5)$$
$$\mathcal{R}_i^2 = d_1 + d_2 \delta_i + \mathcal{E} . \qquad (6)$$

where the index i refers to a galaxy lying at a point $\mathbf{r}_i$ with smoothed density δ_i. The residuals, $\mathcal{R}$, and $\mathcal{E}$ are random numbers with zero mean values and the parameters c_2 and d_2
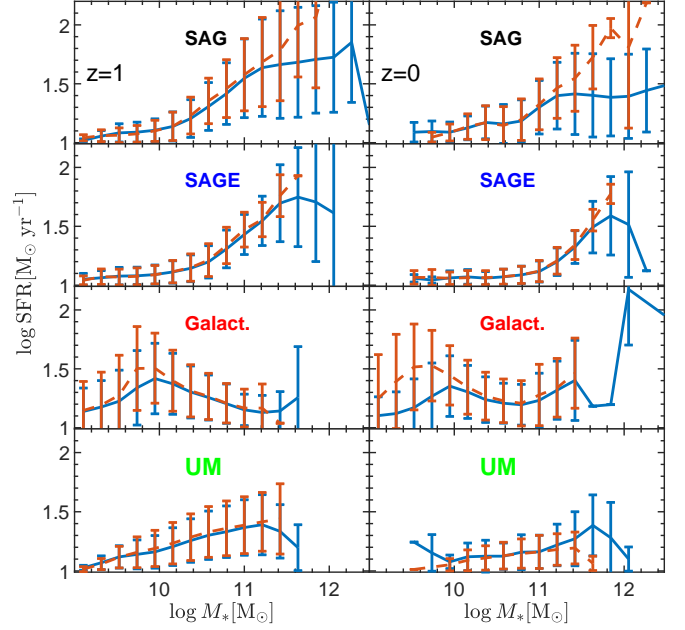

Figure 8. The mean $\log \mathrm{SFR}$ at a given M_* for galaxies with SFR > 10 $M_\odot$ yr^{-1}. Red dashed and blue solid lines correspond to galaxies in the 20% least and most dense regions. Error bars represent scatter around the mean. The TH smoothing width for this plot only is $R_s = 8$ h^{-1} Mpc

.

describe how the mean and variance of $\log \mathrm{SFR}$ vary with the environment density. For galaxies with densities δ_i close to a certain δ_0, the mean and variance are

$$\overline{\log \mathrm{SFR}}|_{\delta_0} = c_1 + c_2 \delta_0 , \qquad (7)$$

and

$$\sigma^2_{\log \mathrm{SFR}}|_{\delta_0} = d_1 + d_2 \delta_0 . \qquad (8)$$

The mean of $\log \mathrm{SFR}$ over all galaxies is, however,

$$\overline{\log \mathrm{SFR}} = c_1 + c_2 \overline{\delta_i} . \qquad (9)$$

The average, $\overline{\delta} = \sum_i \delta_i / N_{\mathrm{gal}}$ of δ_i over *all galaxies* is close to zero, but not strictly so. To evaluate it we work in the continuous limit $\sum_i (\cdot) \to \int \mathrm{d}^3 r n(\mathbf{r})(\cdot)$ where $n(\mathbf{r}) = \bar{n}(1 + \delta_{\mathrm{gal}})$ with $\bar{n}$ the mean number density of galaxies. We find,

$$\overline{\delta} = \langle \delta \delta_{\mathrm{gal}} \rangle_{\mathrm{vol}} , \qquad (10)$$

where the volume average on the r.h.s is over the product of the smoothed mass density times the un-smoothed density inferred from the galaxy distribution, and we have made use of the vanishing volume average of δ. Therefore,

$$c_1 = \overline{\log \mathrm{SFR}} - c_2 \langle \delta \delta_{\mathrm{gal}} \rangle \approx \overline{\log \mathrm{SFR}} . \qquad (11)$$

where in the last step it is assumed that the density rms is $\sigma_\delta \ll 1$ and that c_2 is sufficiently small. Similarly,

$$d_1 \approx \sigma^2_{\mathcal{R}} \approx \sigma^2_{\log \mathrm{SFR}} . \qquad (12)$$

In practice, we first estimate c_1 and c_2 from the mocks by an ordinary least square fitting to $\log SFR_i$. Then the two parameters are used to compute the residual $\mathcal{R}_i$ for every galaxy. Finally, the parameters d_1 and d_2 are derived by least square fitting to $\mathcal{R}_i^2$ given from the previous step. The results are summarized in Table 3 for all mock galaxies at $z = 1$ and with SFR > 10 $M_\odot$ yr^{-1}. The entry for each mock lists the inferred parameters for the smoothing widths $R_s = 20$ and 100 h^{-1} Mpc, respectively, in the top and bottom lines. Because of the relatively small simulation box, results with only $R_s = 20$ h^{-1} Mpc are listed for UM mocks in the SMDPL.

For each model, the parameter c_1 varies very little with R_s and is very close to the corresponding $\overline{\log SFR}$ (second column), consistent with Eq. 11. The parameter c_2 which is indicator for the modulation of the mean of $\log SFR$ versus δ, exhibits some dependence on R_s and, as expected, has a small amplitude. Also $d_1 \approx \sigma_{\log SFR}^2$, as expected.

For SAG and GALACTICUS, c_2 has similar values for the two values of R_s. The remaining two models, SAGE and UM, yield stronger dependence on R_s with difference of more than more than 50% in c_2.

The GALACTICUS mock stands out in two respects, it has the strongest sensitivity to the environment (largest $|c_2|$), and, in accordance with Figs. 7 & 6, exhibits an inverted dependence on δ (negative c_2). The results are a function of the SFR threshold, but we find similar numbers for SFR > 12 $M_\odot$ yr^{-1}. For example, the inverted dependence in GALACTICUS persists to SFR > 12 $M_\odot$ yr^{-1} with $(c_2, d_2) = (-0.0371 \pm 0.0007, -0.005 \pm 0.0002)$ and $(-0.036 \pm 0.0004, -0.0031 \pm 0.0015)$, respectively for $R_s = 20$ and 100 h^{-1} Mpc. This model shows the strongest change with the SFR threshold. Parameters in the other mocks change at $< 15\%$.

4. GALAXY BIASING AS A FUNCTION OF THE SFR

Assume we have a (volume limited) sample of N_{gal} galaxies with positions $\mathbf{r}_i$ in a large volume V. Theoretically, the number density contrast δ_{gal} is expressed in terms of a sum over Dirac delta functions

$$\delta_{gal} = \frac{V}{N_{gal}} \sum_{i=1}^{N_{gal}} \delta^D(\mathbf{r} - \mathbf{r}_i) - 1 . \quad (13)$$

This form, although of little practical use, stresses the importance of shot noise resulting from the discrete nature of the distribution of galaxies. Practically, we generate a galaxy density field from each simulation output, by interpolating the galaxy distribution on a cubic grid using the Cloud-in-Cell (CIC) scheme. The grid size is and 256^3 for SMDPL, 512^3 for MDPL2 and 470^3 for BigMDPL. Here also we use galaxies with $M_* > 5 \times 10^9 M_\odot$ and SFR > 10 $M_\odot$ yr^{-1}.

We make various comparisons between galaxy and mass density fields on the grid. A visual impression of the bias-

ing relation is offered in terms of a scatter plot of δ_{gal} vs δ in Fig. 9. For clarity only a small fraction of the densities on the grid are plotted as the blue points. The contour lines mark the boundaries containing 68%. 90% and 95.4% of the points. The contours were computed by fitting a 2D gaussian normal PDF to the distribution of points in the plane $\delta - \delta_{gal}$. The dashed and dash-dotted lines represent, respectively, the linear regression of δ_{gal} on δ and vice versa. Using the expressions in §B, in which we discuss the details of the regression procedure, the slope of the simple linear regression of δ_{gal} on δ is given by

$$p = \frac{\sum \delta_\alpha \delta_{gal,\alpha}}{\sum \delta_\alpha} , \quad (14)$$

where the subscript α refers to grid points. If the biasing relation is indeed well described by Eq. 1, then the ensemble average of this expression is approximated as $\langle p \rangle = b$ thanks to $\langle \delta \varepsilon \rangle = 0$. Therefore, the slope of the dashed lines in the figure should serve as a statistically unbiased estimate of b. The statistical 1σ uncertainty on the slope is given by

$$\sigma_p^2 = \frac{\sum (\delta_{gal,\alpha} - p\delta_\alpha)^2}{N_1 \sum \delta_\alpha^2} , \quad (15)$$

where N_1 is the number of independent grid points. Since the densities are smoothed on a grid, we need to consider that only a fraction of the points are statistically independent. We estimate the number of independent grid points as $N_1 \sim (3/4\pi)(L/R_s)^3$ and apply the expression in Eq. 15 using density values at N_1 randomly selected grid points. This gives $\sigma_p \approx 0.006$ and 0.015, respectively, for the smaller and larger R_s. Thus, the bias factors, $b = 1.44$ and 1.43, estimated as the slopes of the dashed lines in the two panels of Fig. 9 are consistent within the 1σ statistical error.

Given the inferred slopes, the variance of the stochastic term ε in Eq. 1 is estimated as $\sigma_\varepsilon^2 = \text{Var}(\delta_{gal} - p\delta)$. For $R_s = 100$ h^{-1} Mpc, we find $\sigma_\epsilon^2 = 1.1 \times 10^{-4}$, which includes shot noise and intrinsic scatter in the bias relation. Following §A, the shot noise contribution in this case is $\sigma_{SN}^2 = 7.3 \times 10^{-5}$. Since $\sigma_\delta^2 = 1.75 \times 10^{-3}$ and $\sigma_{\delta_{gal}}^2 = 3.7 \times 10^{-3}$ are much larger than σ_ϵ^2, the inverse regression of δ on δ_{gal} leads to a similar slope. The same conclusion applies to $R_s = 20$ h^{-1} Mpc where $\sigma_\epsilon^2 = 1.18 \times 10^{-2}$, $\sigma_{SN}^2 = 9.3 \times 10^{-3}$, $\sigma_\delta^2 = 6.2 \times 10^{-2}$ and $\sigma_{\delta_{gal}}^2 = 1.4 \times 10^{-1}$.

The relation in Eq. 1 is assumed to hold between between the density field on any scale as long as it is large enough. Decomposing the fields in Fourier modes, the relation yields

$$\delta_{gal,k} = b\delta_k + \epsilon_k . \quad (16)$$

We examine now the power spectra $P_g(k) = \langle |\delta_{gal,k}|^2 \rangle$ of the galaxy distribution and $P_{DM}(k) = \langle |\delta_k|^2 \rangle$ of the corresponding dark matter density field. We FFT the un-smoothed δ_{gal} and δ on the grid into Fourier space and compute the respective power spectra. We remove the contribution, N_{gal}^{-1}, of

Table 3. The parameters of the fitting formulae in Eqs. 5 & 6 for a threshold SFR > 10 M$_\odot$ yr^{-1}

	$\overline{\log \mathrm{SFR}}$	c_1	c_2	$\sigma^2_{\log \mathrm{SFR}}$	d_1	d_2
SAG	1.2926	1.2899 ± 0.0002	0.0213 ± 0.0005	0.0634	0.0614 ± 0.0001	0.0151 ± 0.0003
		1.2925 ± 0.0001	0.0263 ± 0.0033		0.0633 ± 0.0001	0.0175 ± 0.0019
SAGE	1.2566	1.2553 ± 0.0001	0.0132 ± 0.0003	0.0343	0.0340 ± 0.0001	0.0030 ± 0.0001
		1.2566 ± 0.0001	0.0174 ± 0.0021		0.0343 ± 0.0001	0.0033 ± 0.0005
Galacticus	1.3598	1.3644 ± 0.0002	-0.0428 ± 0.0007	0.0699	0.0705 ± 0.0001	-0.0066 ± 0.0002
		1.3599 ± 0.0002	-0.0444 ± 0.0044		0.0699 ± 0.0001	-0.0045 ± 0.0015
UM SMDPL	1.2724	1.2724 ± 0.0004	-0.0005 ± 0.0015	0.0416	0.0416 ± 0.0001	0.0002 ± 0.0005
		$-$	$-$		$-$	$-$
UM MDPL2	1.2676	1.2665 ± 0.0001	0.0086 ± 0.0004	0.0414	0.0411 ± 0.0001	0.0014 ± 0.0001
		1.2676 ± 0.0001	0.0049 ± 0.0024		0.0413 ± 0.0000	0.0003 ± 0.0008

the shot noise from the galaxy power spectrum P_{g} (Peebles 1980). Thanks to the large number of DM particles in the simulation, shot noise is negligible in P_{DM}.

In Fig .10, we plot the ratio of the galaxy to the DM power spectra for the various mocks at $z = 0$ (blue curves) and $z = 1$ (red). The Nyquist frequency $k_{\mathrm{N}} = \pi N/L = 1.6$ h Mpc^{-1} and 2.0 h Mpc^{-1} for MDPL2 and MDPL2, respectively. The UM curves are noisier than the others due to to the significantly smaller number of UM mock galaxies (c.f. Table 2). The decline of the ratio at $\log k \gtrsim -0.5$ for mocks from the MDPL2 simulation (i.e. all curves except UM) is due to aliases of the CIC interpolation. Since we are interested in the large scale regime, we have not made any special effort to correct for these aliases (e.g. Jing 2005). The power spectrum ratio versus the wavenumber, k, is an indication to the dependence of the bias factor on scale. For all models, the figure clearly demonstrates a very weak dependence on k in the range $-2 < \log k < -1$, strongly motivating linear biasing. At $z = 0$ (blue) the ratio is larger than unity only for UM. In the remaining models at this redshift, the ratio is less than unity, meaning that the galaxy distribution is less clustered than the dark matter.

It is interesting to examine the biasing relation as a function of the threshold imposed on SFR. We compute the bias factor according

$$b^2 = \frac{\overline{P_{\mathrm{gal}}}}{\overline{P_{\mathrm{DM}}}} \qquad (17)$$

where the overline refers to the average of the power spectrum over the range $-2 < \log k < -1$. Fig. 11 plots b as a function of a lower threshold imposed on the SFR. The bias factor of galaxies with very low SFR (quenched star formation) is highest. These galaxies tend to live in massive halos and thus are strongly biased (clustered). Actively star forming galaxies are associated with less massive halos with lower b, as seen in Fig. 11 for all models. As soon as star formation is active, the the bias factor is nearly constant versus the SFR threshold with GALACTICUS showing the strongest dependence. This is in agreement with Angulo et al. (2014)

who analysed the biasing of SFR selected galaxies extracted from the Millennium-XXL simulation Angulo et al. (2012) using the L-Galaxies SAM Springel et al. (2005). Based on the galaxy and DM correlation functions at separations $60 - 70$ h^{-1} Mpc, they find that the bias factor depends weakly on the SFR (expressed in terms of number density in their case) with $b \approx 1.1$ and .7, respectively, at $z = 1$ and $z = 0$. In Fig. 11, these values are best matched by the SAGE galaxies, while the other SAMS predict larger b values.

The mean stellar mass for the UM mock galaxies with SFR > 10 M$_\odot$ yr^{-1} at $z = 0$ is $M_* = 7.9 \times 10^{10}$M$_\odot$ and we find a similar value $M_* = 5 \times 10^{10}$M$_\odot$ for SAG. For these values of M_* the corresponding halo mass in the models is $\sim 2 \times 10^{12}$M$_\odot$ with a factor of 2 scatter (cf. Fig. 8 in Knebe et al. 2018). According to Comparat et al. (2017) who analyzed halo bias in the MULTIDARK simulations, the relevant bias for this halo mass range is around unity with some scatter. Taking into account the range of the halo mass and the scatter in the biasing relation, we find the difference in b, measured from the slopes in Fig.9 and $P_{\mathrm{gal}}/P_{\mathrm{DM}}$ between UM and the other models is completely reasonable.

5. THE GROWTH RATE FROM THE SPEED-FROM-LIGHT METHOD (SFLM)

Redshift surveys provide "observed redshifts", z, of galaxies. LOS peculiar velocities introduce a shift between z and the cosmological redshifts z_{c} according to (Sachs & Wolfe 1967),

$$\frac{z - z_{\mathrm{c}}}{1 + z} \approx \frac{V}{c} , \qquad (18)$$

where V is the physical peculiar velocity of a galaxy, the speed of light is c and we have neglected terms related to the gravitational potential and higher order in V/c. Further, we will not consider the important effect of magnification by gravitational lensing in this paper (cf. §C for some considerations of this effect).

Cosmological redshifts can only be derived from actual distances and, therefore, are impossibles to measure for most
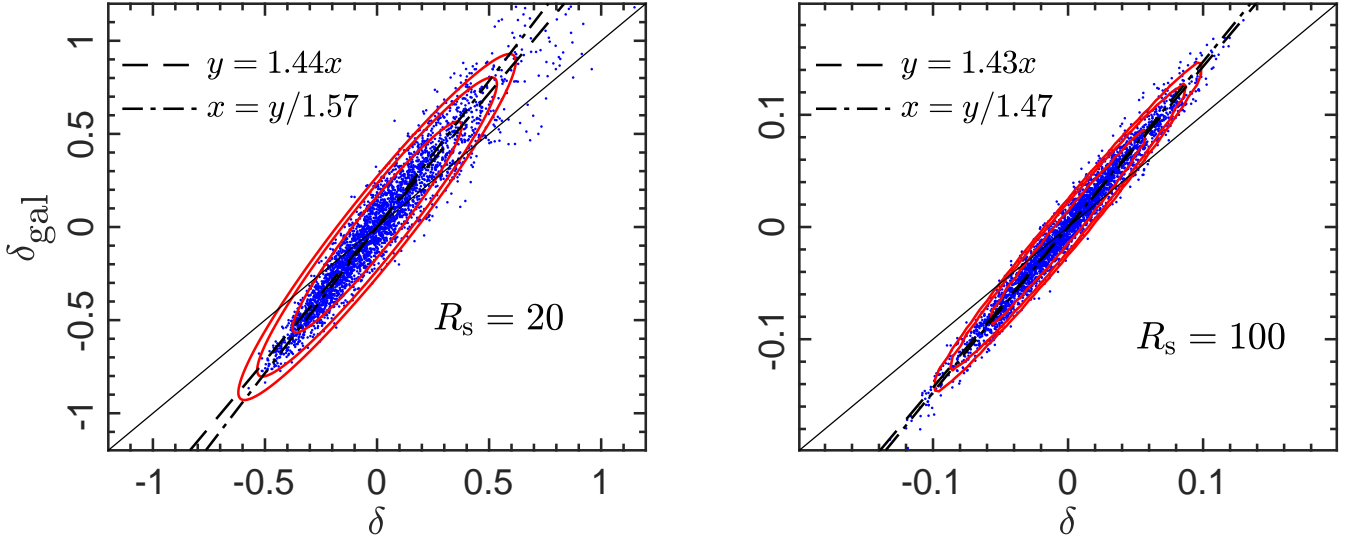
Figure 9. Scatter plot of the smoothed galaxy versus DM density fields for the $z = 1$ SAG galaxies. Left and right panels correspond, respectively to TH smoothing of widths $R_s = 20$ and 100 h^{-1} Mpc. Slopes obtained via linear regression of $\delta_{\rm gal}$ on δ and vice versa are plotted as the dashed and dash-dotted lines, respectively, and indicated in the labels. To guide the eye, the diagonal line $\delta_{\rm gal} = \delta$ is plotted in thin solid
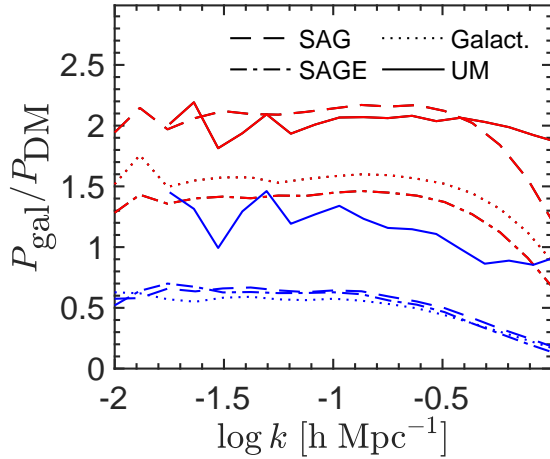

Figure 10. The ratio of the galaxy to the DM power spectrum at $z = 1$ (red curves) and $z = 0$ (blue). Only the full UM in SMDPL is plotted.

Figure 11. The bias factor computed using Eq. 17 of galaxies with SFR above a limiting value. Red and blue curves correspond to $z = 1$ and $z = 0$, respectively.

galaxies in redshift surveys. Therefore, the (luminosity) distances, $d_{\rm L}$ computed at z rather than $z_{\rm c}$, are used to derive SFRs and stellar masses of galaxies from the observed fluxes. This obviously holds for the derivation of any intrinsic luminosity of galaxies, but we will phrase the relevant relations in terms of the SFR.

Given the measured flux, F, the observed SFR is given by

$$\mathrm{SFR}_{\rm obs} = 4\pi d_{\rm L}^2(z)F \; . \qquad (19)$$

The true intrinsic SFR is instead (cf. §C)

$$\mathrm{SFR} = 4\pi d_{\rm A}^2(z_{\rm c})(1+z)^4 F \; , \qquad (20)$$

where $d_{\rm A}(z_{\rm c}) = d_{\rm L}(z_{\rm c})/(1 + z_{\rm c})^2$ and similarly for $d_{\rm A}(z)$, is the angular diameter distance. Collecting up the terms, we write

$$\log \mathrm{SFR}_{\rm obs} = \log \mathrm{SFR} + \mathcal{V} \; , \qquad (21)$$

with

$$\mathcal{V} = 2\log\left[\frac{d_{\rm A}(z)}{d_{\rm A}(z_{\rm c})}\right] \; . \qquad (22)$$

In §C we show that to first order in V,

$$\mathcal{V} \approx \frac{V}{c}\mathcal{D}(z) \; , \qquad (23)$$

where

$$\mathcal{D}(z) = 0.868 \left[\frac{c}{H(z)d_A(z)} - 1 \right] . \qquad (24)$$

The different signs for the two terms in the square brackets reflect the fact that the corrections for relativistic beaming and the shift in $d_L(z)$ are in opposite directions. For a given V, the first term is $\sim V/cz$ for $z \ll 1$, while the second term is independent of redshift. At $z = 1$, this gives $\mathcal{V} = 1.4 \times 10^{-4}(V/100\,\mathrm{km\,s^{-1}})$. Lets compare this to the modulation of $\log \mathrm{SFR}$ due to environmental density dependence. Taking the parameter $c_2 = 0.026$ from Table 3 for SAG as an example. The density rms for $R_s = 100\,\mathrm{h^{-1}\,Mpc}$ is $\sigma_\delta = 0.042$. Thus the modulation in the mean $\log \mathrm{SFR}$ versus the environment density is typically $c_2\sigma_\delta = 10^{-3}$. This is almost an order of magnitude larger than $\mathcal{V}$. Thus, as expected, at $z \sim 1$, in the ΛCDM framework the SFLM cannot be used as a direct probe of V as was done at $z \ll 1$ for 2MRS and SDSS by Branchini et al. (2012); Feix et al. (2015, 2017). Of course, it can still be useful for constraining non-standard models predicting unusually large amplitude of the velocity field at high redshift.

But now let us focus on the SFLM method. The distribution of galaxies in the redshift survey, allows a reconstruction of the peculiar velocity field. Linear theory of gravitational instability relates the 3D physical velocity field, $\mathbf{v}$ to the mass density field in *real (comoving distance) space* as

$$\nabla^2\phi = aHf(\Omega)\delta \qquad (25)$$
$$\approx aH\beta\delta_{\mathrm{gal}} , \qquad (26)$$

where we assume a potential flow, $\mathbf{v} = -\nabla\phi$, and adopted a linear biasing relation Eq. 1 with negligible scatter to arrive at the second line. The solution to this Poisson equation is obtained from the galaxy distribution as a function of a single parameter[3] β in Eq. 3 The spatial derivative in the relations Eqs. 25 & 26 is with respect to the comoving distance coordinate, $\mathbf{r}$, and the density fields are assumed in real space. In the application to redshift surveys, Eq. 26 needs to be modified to account for the difference in the comoving distance being derived from the observed redshift z rather than the cosmological redshift z_c. Denoting the galaxy density in *redshift space* by $\delta_{\mathrm{gal}}^{\mathrm{red}}$, the equation becomes (e.g. Nusser & Davis 1994),

$$\nabla^2\phi + \frac{\beta}{r^2}\frac{\partial}{\partial r}\left(r^2\frac{\partial\phi}{\partial r}\right) = aH\beta\delta_{\mathrm{gal}}^{\mathrm{red}} . \qquad (27)$$

We see that the degeneracy between f and b is maintained and the solution remains only a function of β. There is an important difference though; the solution is not linearly proportional to β, and the equation needs to be solved for every

---

[3] The parameter H disappears from the equation if distances are expressed in $\mathrm{km\,s^{-1}}$.

---

value of β of interest (cf. Nusser & Davis 1994, for details). Non-linear effects are important on small scales, especially in redshift space where incoherent motions and finger-of-god effects smear out structure in the los direction. However, we are interested in tens of Mpc scales where linear theory is completely satisfactory for the purpose of recovering the peculiar velocity (Keselman & Nusser 2016). The tests we perform below are tailored to the expected uncertainties from the finite number of particles and environmental density effect. Thus, for simplicity of presentation and clarity of the results, we choose to work with real space density fields and thus we only use velocity reconstructed from Eq. 26.

The SFLM seeks β as the value that renders a minimum in the function

$$\tilde{\chi}^2(\beta) = \sum_{i\in\mathrm{gal}} \left[\log \mathrm{SFR}_{i,\mathrm{obs}} - \mathcal{V}_i(\beta)\right]^2 . \qquad (28)$$

We will assume the approximate expression $\mathcal{V} = V\mathcal{D}/c$ (see Eq. 23) and that the velocity model is linear in β. We also assume that we are given the velocity field V_1 corresponding to a solution Eq. 26 with a fixed value for $\beta = \beta_1$. Thus, $\mathcal{V}(\beta) = \beta\mathcal{V}_1/\beta_1$ and the problem reduces to a simple linear regression as described in §B. The minimum condition $\partial\tilde{\chi}^2/\partial\beta = 0$, gives

$$\frac{\beta}{\beta_1} = \frac{\sum_i \Delta\mathcal{V}_{i,1}\,\Delta\log\mathrm{SFR}_{i,\mathrm{obs}}}{\sum_i(\Delta\mathcal{V}_{i,1})^2} . \qquad (29)$$

We have defined

$$\Delta\mathcal{V}_{i,1} = \mathcal{V}_{i,1} - \overline{\mathcal{V}}_1 \qquad (30)$$

where an over-line indicates a mean over galaxies in the sample and the same definition applies to $\log\mathrm{SFR}_{\mathrm{obs}}$. The 1σ error on β is given by

$$\frac{\sigma_\beta^2}{\beta_1^2} = \frac{\sum_i\left(\Delta\log\mathrm{SFR}_{i,\mathrm{obs}} - \frac{\beta}{\beta_1}\Delta\mathcal{V}_{i,1}\right)^2}{N_{\mathrm{gal}}\sum_i(\Delta\mathcal{V}_{i,1})^2} , \qquad (31)$$

where N_{gal} is the number of galaxies.

5.1. *A rough estimate of the error*

Before we present full results for the expected errors on β we give here a rough estimate. This is most easily achieved if we take $\log\mathrm{SFR}_{\mathrm{obs}} = \log\mathrm{SFR}$, so that minimization of the function $\tilde{\chi}^2$ should yield β consistent with zero for a model of the form $\mathcal{V}(\beta) = \beta\mathcal{V}_0$, where $\mathcal{V}_0$ is computed from the true peculiar velocities (cf. Eq. 22). Of course, in reality $\mathcal{V}$ will be obtained from the velocities recovered from δ_{gal}, but we are only interested in a rough estimate in this section.

Galilean invariance implies the absence of correlation between the properties of galaxies and their velocities. Therefore, the ensemble average of Eq. 29 over all possible realizations of $\log\mathrm{SFR}_i$ yields $\langle\beta\rangle = 0$.. This is valid even if the

star formation depends on the underlying mass density since the velocity and density are also uncorrelated. An estimate of the variance of the scatter around $\langle\beta\rangle = 0$, is

$$\sigma_\beta^2 \equiv \langle\beta^2\rangle = \frac{1}{N}\frac{\sigma_{\log\,\mathrm{SFR}}^2}{\sigma_\mathcal{V}^2}\ . \tag{32}$$

where $\sigma_\mathcal{V}^2 = \overline{(\mathcal{V}-\overline{\mathcal{V}})^2}$ and $\sigma_{\log\,\mathrm{SFR}}^2 = \langle(\log\mathrm{SFR} - \langle\log\mathrm{SFR}\rangle)^2\rangle$. In the limit of a large number of objects $\sigma_{\log\,\mathrm{SFR}}^2 = \overline{(\log\mathrm{SFR} - \overline{\log\mathrm{SFR}})^2}$. At $z = 1$, Eq. 22 gives $\mathcal{V} = 4.2\times 10^{-4}(V/300)$. For the SAG mock galaxy catalogs, $\sigma_{\log\,\mathrm{SFR}} \approx 0.25$ for SFR > 10 $\mathrm{M_\odot yr^{-1}}$. Thus

$$\sigma_\beta = 0.13\left(\frac{2\times 10^7}{N}\right)^{0.5}\left(\frac{300\,\mathrm{km\,s^{-1}}}{\sigma_V}\right) \tag{33}$$

At $z = 1$, the simulations give $\sigma_V = 300\,\mathrm{km\,s^{-1}}$ for the 1D rms of unfiltered galaxy velocities.

5.2. *Recovered vs. true velocities: smoothing matters*

The rough error estimate presented above is based on the true los velocities, while in a realistic application only the reconstructed los velocities, V_rec, from the galaxy distribution smoothed on a large scale are available. Therefore, the β estimate from the SFLM is basically the slope of the regression of the true $\mathcal{V} = \mathcal{D}V/c$ in Eq. 21 on the reconstructed $\mathcal{V}_\mathrm{rec} = \mathcal{D}V_\mathrm{rec}/c$, where $\mathcal{V}$ is perturbed by the random spread in $\log\mathrm{SFR}$.

Smoothing alone causes a statistical bias in the estimate of the slope (β), i.e. even if the smoothed true velocities, V_s where used instead of V_rec, we expect a slope of the regression of V on V_s to differ from unity due to the correlation between $V - V_\mathrm{s}$ and V_s for the TH smoothing.

In this section we explore the expected statistical bias in the estimates of the slope. We begin with a basic assessment of ability of the linear theory relation, Eq. 25, at reconstructing the peculiar velocity from the DM density field, δ. In Fig. 12 Cartesian velocity components V_rec reconstructed from δ with the true value of the parameter f are plotted against the true velocities, V. Both V_rec and V are provided on a grid and have been smoothed with a TH window of width $R_\mathrm{s} = 20$ (left panel) and 100 $\mathrm{h^{-1}\,Mpc}$ (right panel). For clarity, only a small randomly selected fraction of the grid points is plotted. This figure refers to the $z = 1$ output from the MDPL2 simulation. Linear theory in this case performs extremely well. The slopes of of the regression of V_rec on V as well as that of the inverse regression, are clearly very close to unity. Further, the scatter in V_rec versus V is negligible even for the smaller smoothing.

Next we turn to reconstruction from the galaxy density field, using Eq. 26 with $\beta = f$. The results are shown in

Fig. 13 for the $z = 1$ SAG galaxies selected above the Euclid cut SFR > 10 $\mathrm{M_\odot}$ $\mathrm{yr^{-1}}$ (cf. Table 2). The contours contain 68%. 90% and 95.4% of the points, obtained by fitting a 2D normal PDF to the distribution of points in the $V_\mathrm{rec} - V$ plane. The results are quite different from the previous figure. The regression slopes clearly deviate from unity in this case. Since V_rec is derived for $\beta = f$, the slope of the regression of V_rec on V should yield the galaxy bias factor, b. Indeed, the slope is very close to the values obtained from the density scatter plot in Fig. 9 and from the ratio of the power spectra as seen in Fig. 10 & Fig. 11 for SAG.

We know already from Fig. 12 that inaccuracies associated with linear theory reconstruction on the scales considered are negligible. That implies that the origin of the scatter in Fig. 13 is stochasticity in the biasing relation and the effect of shot noise on V_rec. The rms of the residual between V_rec and the best fit lines (dashed curves) in Fig. 13 is $63.4\,\mathrm{km\,s^{-1}}$ and $26.8\,\mathrm{km\,s^{-1}}$ for $R_\mathrm{s} = 20$ and 100 $\mathrm{h^{-1}\,Mpc}$, respectively. To quantify the contribution of the shot noise we resort to appendix §A where we derive the following expression for the variance of the shot noise effect on V_rec (see also Strauss et al. 1992)

$$\sigma_{V,\mathrm{SN}}^2 = \frac{(aH\beta)^2}{10\pi\bar{n}R_\mathrm{s}}\ . \tag{34}$$

For SAG at $z = 1$ and $\beta = f$, we find $\sigma_{V,\mathrm{SN}} = 36.4\,\mathrm{km\,s^{-1}}$ and $16.3\,\mathrm{km\,s^{-1}}$ for the smaller and larger R_s, respectively. This makes the contribution of biasing stochasticity $51.9\,\mathrm{km\,s^{-1}}$ and $21.2\,\mathrm{km\,s^{-1}}$, respectively, for the two smoothing widths. Thus, the intrinsic stochasticity in the biasing relation is the dominant contribution to the scatter.

So far we have made comparisons between V_rec and V smoothed on the same scale. In contrast, the model velocity in the SFLM is smoothed, while the data $\log\mathrm{SFR}_\mathrm{obs}$ involves the true galaxy velocities. In Fig. 14 we plot the true un-smoothed SAG galaxy velocities, V_gal, vs V_rec from the galaxy density field. Note that in this plot V_rec is plotted on the $x-$axis.

Only a sharp $k-$cutoff filtering, yields a vanishing correlation between the residual $V_\mathrm{gal} - V_\mathrm{rec}$ and V_rec. However, an idealised sharp $k-$cutoff filtering is impossible to apply to real data due to complicated observational window functions. For the more practical TH smoothing the correlation affects the regression slopes (cf. §B). In addition, as we have seen in Fig. 13, stochastic biasing and shot noise will add scatter to V_rec as recovered from the galaxy density field.

The scatter will also affect the slope but as we have seen the effect is small since both the forward and inverse regression in Fig. 13 have similar slopes. Therefore, it is not surprising that the regression slopes in Fig. 14 are quite different from those in Fig. 13 and from each other. The relevant slope for the SFLM is that of the regression of V_gal on V_rec. For both smoothing the slopes are closer to unity than the obtained
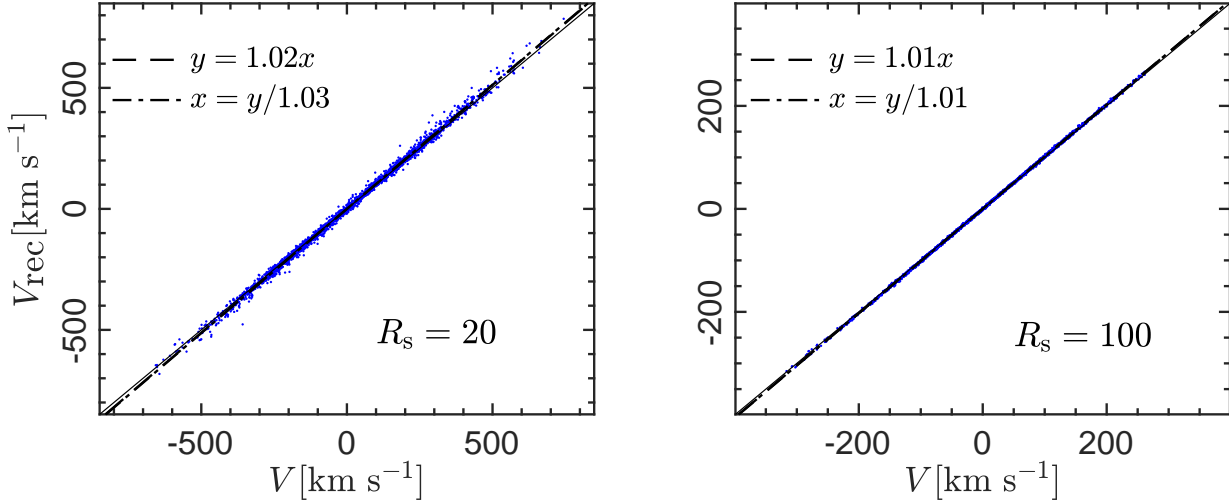
Figure 12. Comparison between the velocity predicted from the DM density field using the linear relation Eq. 25. Both velocity fields are given on a grid and smoothed with a tophat window of width 20 h^{-1} Mpc (left) and 100 h^{-1} Mpc (right), as indicated in the figure. For clarity, only a small fraction of the grid points are shown as the blue dots. Dashed and dash dotted lines represent linear regression of V_{pred} on V and its inverse. The slopes are indicated in the plots. The diagonal (thin solid) is plotted to guide the eye.
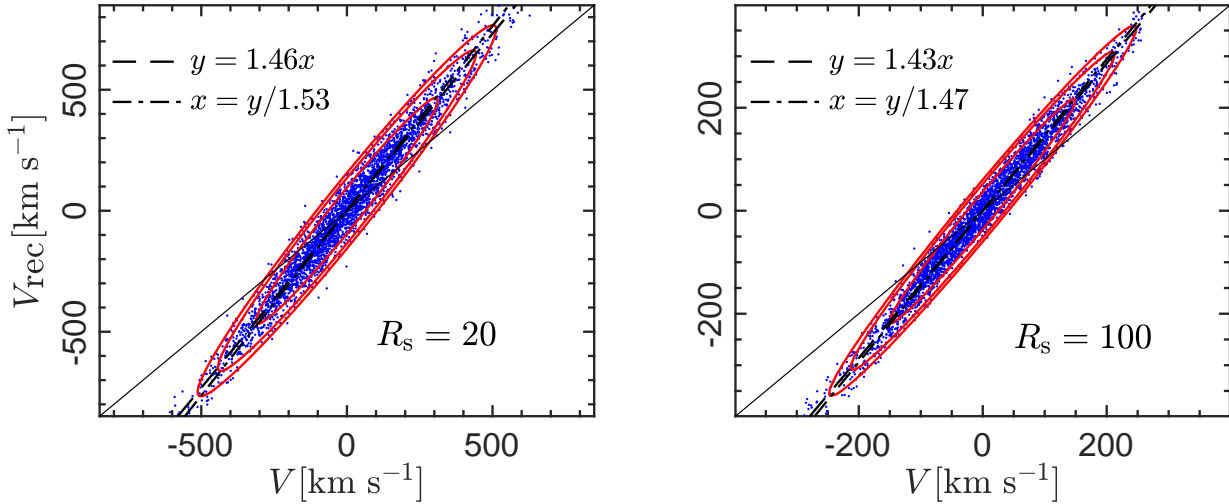
Figure 13. Same as the previous figure but for V_{pred} from the galaxy density field in the SAG simulations. Red contours enclose %68, %90 and %95 of the points. The slope of the dashed line is consistent with the bias factor for SAG galaxies with $SFR_{lim} \approx 10$ in Fig. 11 (dashed curve).

by a regression of the identical smoothing case of V on V_{rec} in Fig. 13. Just for comparison, the slope of V_{rec} on V_{gal} is 4.22 for $R_s = 100$ h^{-1} Mpc and is 1.43 for the identical smoothing case in the right panel of Fig. 13.

Therefore, in order to infer a statistically unbiased β estimate, one should carefully calibrate the result to account for the inherently different smoothing between the models and the data. The same point also has been repeatedly emphasised in regard to the velocity-velocity comparison local surveys by Nusser & Davis (1995); Davis et al. (2011a, 1996).

5.3. *Tests of* SFLM *with mock catalogs*

We are now in a position to present the results of our tests of the SFLM applied to mock catalogs and its sensitivity to SFR and environment. This exercise is to be viewed as an intermediate phase testing of the SFLM towards detailed forecast and full application to realistic surveys. Therefore, we do not make any attempt to run the tested on mock catalogs generated in light cones matching the expected number of galaxies vs redshift. Instead, we simply place the simulation
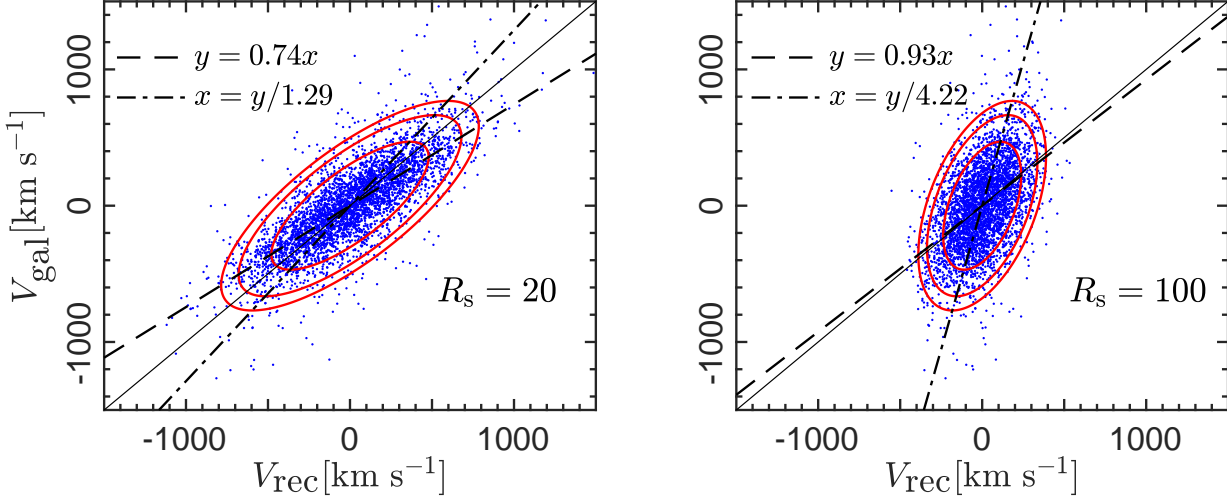
Figure 14. The actual galaxy velocities versus the prediction from the relation using the galaxy density field smoothed on $R_s = 20$ and $100\ h^{-1}$ Mpc. In contrast to Fig .13 the galaxy velocities here are the raw un-smoothed galaxy velocities. The three velocity components are compared for 1/15000 of the SAG mock galaxies.
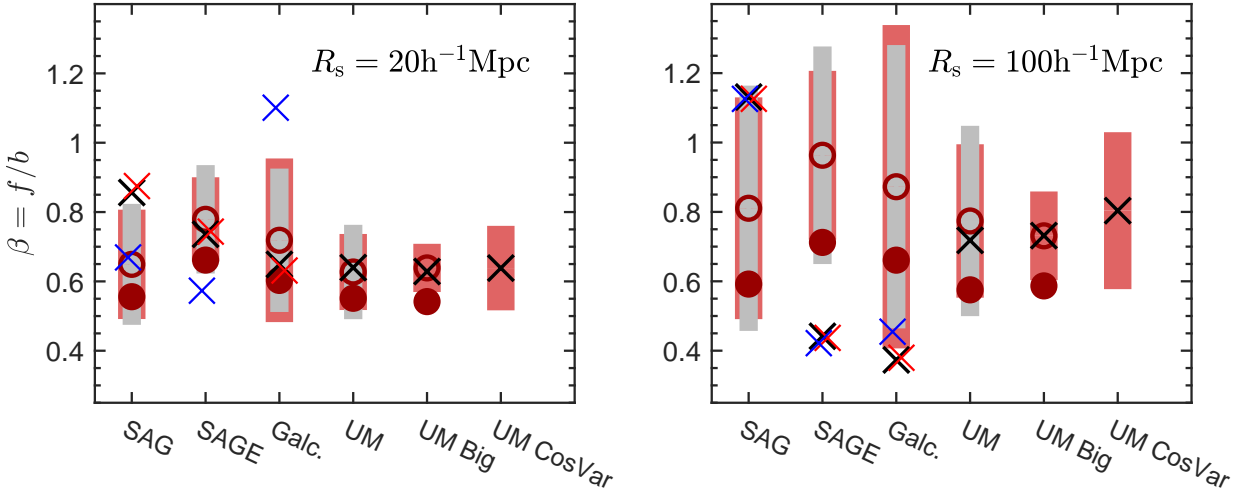

Figure 15. The slope of the regression of $\log \text{SFR}_{\text{obs}}$ on the peculiar velocity estimated using Eq .25 from the galaxy distribution is shown as the crosses for various mocks. Except for the last point to the right in each panel. The error bars represent the rms uncertainty due to the scatter in the SFR distribution. The last point, UM CosVar, also includes cosmic variance expected for a volume of $1h^{-1}$ Gpc. Left and right panels correspond to velocities recovered from the galaxy density field smoothed on 20 and 100 h^{-1} Mpc TH smoothing, as indicated.

box at $z = 1$ and apply SFLM to the simulated sample[4] (c.f. §2.2). For the sake of conciseness we define β_{SFLM} as the β estimate obtained from the application of the SFLM.

Following the discussion in §2.2, since the MDPL2 mocks have substantially smaller volume and less objects than the typical corresponding sample obtained form next-generation surveys, our tests will provide upper bounds on the expected

errors on β from the SFLM. Furthermore, mocks taken from the same MDPL2 parent simulations cannot be used to quantify cosmic variance. For this purpose we resort to UM BigMDPL to quantify the uncertainty in β_{SFLM} due to cosmic variance on the scale of the MDPL2. This is done by partitioning the BigMDPL box into cubic sub-volumes each matching the size of the MDPL2 box. The SFLM is then applied to the mock galaxies in each of these sub-volumes individually. The scatter in the β_{SFLM} values from all the sub-volumes serves as an indication of the cosmic variance on the scale of the MDPL2 box and should serve as an upper

---

[4] For The MDPL2 volume of (comoving) $1(h^{-1}\ \text{Gpc})^3$ is equivalent to the volume of a %5 of the sky between $z = 1$ and 1.2. For reference, the sky coverage of Euclid is %35 of the sky

bound on the cosmic variance on the scale of real, upcoming surveys.

The "observed" quantities $\log \mathrm{SFR}_\mathrm{obs}$ are obtained by shifting the true $\log \mathrm{SFR}$ by $\mathcal{V}$, as in Eq. 21. We work with the approximate expression in Eq. 23 for $\mathcal{V}$ and write the model $\mathcal{V}$ as

$$\mathcal{V}(\beta) = \frac{\beta}{f} \mathcal{V}_1, \tag{35}$$

where

$$\mathcal{V}_1 = \frac{V_{\mathrm{rec},1}}{c} \mathcal{D} \tag{36}$$

with $V_{\mathrm{rec},1}$ being the reconstructed peculiar velocity V_rec obtained from the galaxy density field δ_gal, as a solution to Eq. 26 for $\beta = f(\Omega)$. Solutions are provided for a TH smoothing of δ_gal with widths of $R_\mathrm{s} = 20$ and $100\ \mathrm{h}^{-1}\ \mathrm{Mpc}$, respectively. In all cases we impose $\mathrm{SFR} > 10\ \mathrm{M}_\odot\ \mathrm{yr}^{-1}$ and consider the three Cartesian components of the true raw velocities of galaxies, $\mathbf{v}_\mathrm{gal}$, to obtain three sets of $\log \mathrm{SFR}_\mathrm{obs}$, respectively. Thus for each mock, we have three values of β_SFLM corresponding to the three Cartesian components. In the results referring to MDPL2 mocks we consider the mean of the three values for each mock. Since the three components of the velocity are statistically independent, we effectively are assessing the SFLM with a number of objects which is triple what we actually have in each mock. The increase in the statistical sampling should yield a more reliable error estimate to be used as an indicator to precision that can be achieved with $\mathcal{O}(10^7)$ as in the full Euclid's spectroscopic survey.

The β_SFLM values obtained from each set of mocks are summarized in Fig. 15 for $R_\mathrm{s} = 20$ (left panel) and $100\ \mathrm{h}^{-1}\ \mathrm{Mpc}$ (right panel), as indicated in the figure. The labels SAG, SAGE, GALACTICUS on the x-axis, correspond to the MDPL2 mocks generated using the full galaxy formation machinery in each model. UM refers UM mocks in MDPL2, obtained by re-sampling the UM SMDPL galaxies, as described in §2.1. UM Big is the same as UM but for the BigMDPL simulation. UM CosVar show the results obtained from the sub-volumes of UM BigMDPL to assess cosmic variance on the scale of MDPL2.

The different symbols in the plots indicate β_SFLM values and their scatter obtained with different procedures:

- *Empty red circles* (⭕): These are the β values obtained by a regression of the true galaxy velocities on the model V_1. Therefore, these values represent what the SFLM would yield theoretically in the limit of an infinite number of objects. and should be regarded as the reference value for the β parameter.

- *Black crosses* (✕): These are the β_SFLM value obtained from the SFLM method in each mock, averaging over the three Cartesian velocity components For

the UM mocks, they correspond to the average β_SFLM obtained from 20 random re-samplings of the full UM in SMDPL.

- *Filled red circles* (●): These symbols represent $\beta = f/b$ using the true f and b obtained via a regression of the galaxy density on the DM density (both smoothed with the same window, e.g. Fig. 9). Very similar values are obtained for b estimated from the regression of the smoothed $V_{\mathrm{rec},1}$ on the smoothed true velocities (e.g. Fig. 13).

- *Blue crosses* (✕): SFLM β estimates including environmental dependencies using δ in Eq. 37 (see §5.4). They are provided for the SAG, SAGE and GALACTICUS cases only.

- *Red crosses* (✕): These β values are the same as the blue crosses but using δ_gal in Eq. 37 (see §5.4)

- *Red vertical bands* (▮): For all cases except UM CosVar. They represent the 1σ error on β_SFLM, computed according Eq. 31. As stated above, this is the error on the mean of the three values obtained for the three Cartesian components or equivalently from a single β estimated from triple the number of galaxies in each mock. The red bands are centered on the empty red circles.

- *Red vertical bands* (▮): For the UM CosVar case. The bands represent the rms of the β_SFLM values obtained from sub-volumes of the simulation BigMDPL. This scatter accounts for the combined error from cosmic variance and the scatter in $\log \mathrm{SFR}$.

- *Grey vertical bands* (▮): These bands provide a crude estimate of the error expected for a Euclid-like survey, obtained by re-scaling the errors shown as red bands. Their estimate account for a) the number density vs. z given in Table 3 in Euclid Collaboration et al. (2019), b) the monotonic decrease of $\mathcal{D}$ with z in Eq. 24, and c) the dependence of $\sigma_{\log \mathrm{SFR}}^2$ with z as a result of change in the limiting SFR for a given observed flux limit.

The error bars (red and grey bands) for $R_\mathrm{s} = 100\ \mathrm{h}^{-1}\ \mathrm{Mpc}$ (panel to the right) are roughly a factor of two larger than the corresponding errors for $R_\mathrm{s} = 20\ \mathrm{h}^{-1}\ \mathrm{Mpc}$. The smaller smoothing clearly captures more details of the structure of the velocity field and is bound to yield a tighter fit to the data. Quantitatively, the relative difference in the errors can be understood from Eq. 33 taking $\sigma_V = 210$ and $110\ \mathrm{km\,s}^{-1}$ for the small and large R_s, respectively. The increase in the error is consistent with the ratio of σ_V.

The reason for the differences between the empty and filled red circles is explained in §5.2. The empty red circles are regressions of raw on smoothed velocities which

leads to distinct slopes from regressions done with equally smoothed velocities. This accounts for the larger difference for $R_s = 100 \text{ h}^{-1} \text{ Mpc}$ and also the fact that the empty red circles are always above the filled red ones.

Given the red error bars, β_{SFLM} (back crosses) for SAG, SAGE and GALACTICUS are consistent with theoretical values that would be obtained from an infinite number of data points (empty red circles). The largest deviation is for SAGE with $R_s = 100 \text{ h}^{-1} \text{ Mpc}$. We could not identify any specific cause for this $\sim 2\sigma$ deviation. Recovered vs true velocities follow the same correlation as for other models and it seems that this is just a random statistical fluctuation.

The black crosses and the empty red circles for the UM mocks in the fourth and fifth sets, are very similar. This is expected since the SFLM beta values here are averages over many random re-sampling realisations of the original UM in SMDPL. Furthermore, the rms of the scatter in β around the average is consistent with the error computed with Eq. 31.

The red error bar on the set UM CosVar is comparable to the red error bands for the UM set. This is important since it implies that the contribution of the cosmic variance to the error budget is small. The main error is due to the finite number of data points.

The 1σ error on β obtained by averaging the grey bands over SAG, SAGE, GALACTICUS and UM is $\sigma_\beta = 0.17$ and 0.34 for the small and large smoothing widths, respectively. Using the bias factors computed for each mock, the corresponding errors on f are $\sigma_f = 0.22$ and 0.45.

5.4. *Environment in the* SFLM

As already pointed out, environmental dependencies should not introduce systematic errors on β_{SFLM}, only affect the random uncertainty. To prove this statement, we perform a simultaneous SFLM fitting of β and the parameters c_1 and c_2 characterizing environmental dependencies (c.f. Eq. 5). Generalizing Eq. 28, we write

$$\tilde{\chi}^2(\beta, c_1, c_2) = \sum_{i \in \text{gal}} \left(\log \text{SFR}_{\text{obs},i} - \frac{\beta}{f} \mathcal{V}_{1,i} - c_1 - c_2 \delta \right)^2 . \tag{37}$$

The parameters d_1 and d_2 introduce a dependence on the scatter of $\log \text{SFR}$ and do not affect into the description here. They would, however, enter the analysis if each data point $\tilde{\chi}^2$ is assigned a weight according to the expected scatter in $\log \text{SFR}$. Even then the variation of the weighting would be mild at the level of $\sigma_\delta d_2 / \sigma^2_{\log \text{SFR}} < 10\%$, taking $\sigma_\delta = 0.24$ and d_2 values from Table 3.

The minimum is obtained for,

$$\beta = \frac{\sum(\Delta \mathcal{V}_{1,i} \Delta \log \text{SFR}_{\text{obs}\,i} - c_2 \Delta \mathcal{V}_{1,i} \Delta \delta_i)}{\sum \mathcal{V}^2_{1,i}} , \tag{38}$$

$$c_2 = \frac{\sum(\Delta \delta_i \Delta \log \text{SFR}_{\text{obs}\,i} - \beta \Delta \mathcal{V}_{1,i} \Delta \delta_i)}{\sum \delta^2_i} . \tag{39}$$

where the Δ symbol implies that the mean value (over the galaxies) have been subtracted. The parameter c_1 accounts for the fact that the mean of δ over galaxies is not strictly zero, and will not be considered further in our analysis

In realistic applications, only the galaxy density δ_{gal} is accessible to observations, and therefore we repeat the minimization procedure using δ_{gal} instead of δ. The blue and red crosses in Fig. 15 are β_{SFLM} as a solution to Eq. 3 obtained with δ and δ_{gal}, respectively. The results are shown for SAG, SAGE and GALACTICUS only. For the larger smoothing (right panel) the results are very close to the black crosses corresponding to minimizing Eq. 28. The results with δ_{gal} (red crosses) are well within the statistical error for the smaller smoothing. The same is true for the blues crosses for the SAG and SAGE. However, for the small smoothing, the GALACTICUS estimate obtained with δ_{gal} is significantly higher than all other estimates. This is perhaps not surprising since, as mentioned above, the GALACTICUS galaxies are peculiar, exhibiting inverted environmental dependencies.

Since we have tripled the number of fitting parameters relative to the estimates in the previous sections, we should naively expect that the error on β is substantially increased. Lets us examine this issue in detail. Since the ensemble average $\langle \Delta \delta \Delta \mathcal{V} \rangle = 0$, we find that the ensemble averages $\langle \beta \rangle$ and $\langle c_2 \rangle$ in Eqs. 38 & 39 is the same as in the previous section (c.f. Eq. 29). For the same reason, the ensemble average of the error covariance matrix is diagonal. It, therefore, suffices to examine Eq. 38 alone to conclude that the added error due to the term with c_2 is $\mathcal{O}(1/N_{\text{gal}})$ compared to $\mathcal{O}(1/\sqrt{N_{\text{gal}}})$ for the first term. As a result, we find that the computed errors on β estimated with and without the inclusion of c_2 are very close to each other.

6. DISCUSSION

The effects of the large scale environment on galaxy properties have been the focus of numerous observational studies (e.g. Hoyle et al. 2005; Bernardi et al. 2005; Park et al. 2007; Disney et al. 2008; Blanton & Moustakas 2009; Tempel et al. 2011; Hahn et al. 2015). Although the environment has a strong impact on distribution of a single property (e.g. stellar mass), all evidence points that it plays a meagre role in shaping intrinsic relations between galaxy properties such as the fundamental plane and the Tully-Fisher relations (Bernardi et al. 2005; Disney et al. 2008; Nair et al. 2010). Despite the importance of the environmental dependence on these scaling relations has not yet been invoked as a strong constrain on galaxy formation models (but c.f. Mo et al. 2004). Part of the reason is that these relations involve observations which are sensitive to the distribution and kinematics of stars which are not properly followed in the SAM-DM simulations combination. Also, hydrodynamical simulations of galaxy formation may not be large enough

to quantitatively explore this dependence There are, however, certain intrinsic relations that involve properties which can be studies with SAM. Among these, the one we touched upon in this work is the mean SFR at a given stellar mass, shown in Fig. 8 for galaxies with high SFR (> 10 M$_\odot$ yr^{-1}). Our analysis has revealed important differences among various galaxy formation models. The UM and SAGE models showed little evidence for dependence on environment, while in SAG, the SFR is boosted in less dense environment only for stellar masses above 10^{11}M$_\odot$. GALACTICUS galaxies are associated with higher SFR in less dense environments only for $M_* \lesssim 10^{10}$M$_\odot$.

A central goal of this work is to a make an assessment of the SFLM at constraining the parameter β with mock galaxy catalogs that incorporate as much physical effects as possible and focus on star forming, line emitting objects. The application of the method at $z \simeq 1$ relies on the availability of a large number of galaxies in the survey and therefore we have geared the tests toward the next generation spectroscopic surveys, focusing on the Euclid satellite mission.

The SFLM has been criticized on the ground that it could be susceptible to environmental dependencies in the SFR/luminosity distribution. The concern was already raised and addressed in previous papers by two of the current authors (Feix et al. 2014, 2015) who argued that environmental dependencies affects only a direct identification of luminosity spatial modulations with the large scale velocity field. They pointed out that the environment cannot lead to any systematic effect on the estimation of β in terms of fitting a velocity field reconstructed using the spatial distribution of the same galaxies. This is a direct consequence of Galilean invariance which guarantees a vanishing correlation between peculiar velocity and density field at the same point. We have demonstrated this point in §5.4. Environmental dependencies do not bias the β estimate but can potentially contribute to the errors. Our tests demonstrate that this effect is small. Its magnitude can be inferred by comparing the black cross with the empty red circles in Fig. 15.

Ideally, SFLM should be tested with more realistic mock catalogs that mimic the footprint and the selection effects of a specific survey. In this work we have been focusing on the paradigmatic case of the Euclid survey. Unfortunately the available mock catalogs, though highly valuable to identify and assess environmental dependencies, do not cover a sufficiently large volume needed to mimic the full Euclid survey. In absence of publicly available, realistic mock Euclid catalogs, a reasonable compromise is to generate light cone mock data by stacking the available simulation outputs to cover a sufficiently large volume. We leave this for future work. In this paper we have estimated the errors by rescaling those obtained from the available mocks at $z = 1$ (red bands in Fig. 15) to the expected number of galaxies in the Euclid survey

(grey band errors, same figure). We expect the real error to lies in between the grey and red bands.

It is worth emphasizing that the application of SFLM to these spectroscopic surveys will be quite straightforward. Clustering analyses have been focusing on detecting and fitting the BAO peak to extract cosmological parameters. Most of these analyses include reconstruction procedures to enhance the signal-to-noise of the BAO peak by tracing galaxy orbits back to an epoch in which linear theory applies Padmanabhan et al. (2012); Eisenstein et al. (2007). Among these, reconstruction methods based on the cosmological application of the least action principle Peebles (1989); Nusser & Branchini (2000); Sarpa et al. (2019) generate as "byproduct" a model peculiar velocity field at the epoch of observation that can be readily used as input to the SFLM method.

In this paper we have opted to apply the simplest form of the method and avoid performing a full maximum likelihood estimation (MLE) as in Feix et al. (2015). Theoretically, an MLE analysis would exploit the details of the shape of the SFR/luminosity distribution and not only the second moment as is done here. We leave the application of the MLE to the future analysis of more realistic galaxy mocks.

The amplitude of the velocity induced shift is a strong function of redshift. In fact, for a Planck cosmology the net effect vanished at $z = 1.6$ but then will pick up again with an opposite sign, dominated by the beaming effect (the V/c term). Therefore it can be relevant for all those redshift surveys like DESI and Roman-WFIRST that will target galaxies beyond this redshift.

Gravitational lensing by the foreground mass distribution causes a magnification/de-magnification of galaxies in the survey. For a source at $z = 1$, the mass distribution at $z < 1$ causes a 2×10^{-3} shift in the mean $\log$ SFR in spheres of radius 20 h^{-1} Mpc. The amplitude of the effect is close to the environmental dependency estimated from the mocks. It is rather easy to incorporate this effect in the analysis. Suppose the redshift survey spans the redshift range from $z = 1$ to $z = 2$. Let us separate the lensing shift into a contribution from mass distribution at $z < 1$ and another from mass at $z > 1$. The foreground matter at $z < 1$, will cause shift that varies in a specific way with the distance of galaxies in the survey. Lensing induced by matter at $z > 1$ is easy to model using observed galaxy distribution to infer the density field. The spatial coherence of the total lensing contribution will be quite distinct from the shift due to velocities. We therefore expect little covariance between lensing and peculiar velocity-induced effects, which would make the two contributions easy to discern.

As demonstrated in Fig. 12 , non-linear dynamical effects are insignificant and linear theory is quite satisfactory on the scales of interest. Larger information content is captured by the recovered velocity field for smaller smoothing scales.

We have seen that $R_s = 20 \ h^{-1} \, \mathrm{Mpc}$ is adequate for linear theory reconstruction and yields much smaller errors than $R_s = 100 \ h^{-1} \, \mathrm{Mpc}$. The only possible concern is whether V_{rec} smoothed on a $\sim 20 \ h^{-1} \, \mathrm{Mpc}$ scale is contaminated by shot noise contribution when the mean number density is of the order of the one expected in next-generation surveys, i.e. $\bar{n} \sim 5 \times 10^{-4} h^3 \, \mathrm{Mpc}^{-3}$ (Euclid Collaboration et al. 2019). Substituting this value for $\bar{n}$ with $R_s = 20 \ h^{-1} \, \mathrm{Mpc}$ in Eq. 34, yields $\sigma_{V,SN}^2 = (93 \, \mathrm{km \, s^{-1}})^2$. This is larger than contribution of biasing stochasticity, $(51.9 \, \mathrm{km \, s^{-1}})^2$, to the variance of V_{rec} (see §5.2), but significantly smaller than the variance of the smoothed velocity at $z = 1$, $(210 \, \mathrm{km \, s^{-1}})^2$. Therefore, the expected shot noise contribution will be subdominant in the total error budget which is dominated by the scatter in the SFR.

As we have seen, the SFLM method provides an estimate of the β parameter. It is has become customary to express the results on β via the combination $\sigma_{gal,8}\beta = \sigma_8 f$, thus avoiding the appearance of neither b nor β in the result. We find this to be inadequate. In the case of RSD on large scales, for example, according to Kaiser (1987), only β can be directly inferred from the ratio of angular moments of the observed galaxy power spectrum *independently* of any assumptions regarding σ_8 and the shape of the DM power spectrum. The combination $b\sigma_8$ can also be derived in this context, but only by matching the amplitude of the moments to an assumed shape for the DM power spectrum. Once b and β are known, $f\sigma_8$ can easily be derived. Therefore, since the inference of β depends purely on the relative clustering anisotropy and b mainly on the clustering amplitude, it would be prudent to quote the values separately. Although $f\sigma_8$ is the amplitude of the velocity, it is not the parameter responsible for RSD in the galaxy distribution. Quoting only $f\sigma_8$ creates the false impression that it is the primary quantity which governs the RSD phenomenon.

It is instructive to compare the performance of the SFLM in constraining β to other probes. One of those is by means of a comparison of direct observations of galaxy peculiar velocities versus the predicted velocities from the distribution of redshift surveys. This is possible for local data (within distances $\sim 100 \mathrm{Mpc}$). Davis et al. (2011b) performed such a comparison using the SFI++ velocity catalog and 2MRS gravity. They included a full error analysis and found a 1σ uncertainty in β at the level of $\delta\beta \approx 0.05$. A similar uncertainty is found by Pike & Hudson (2005) using different analysis technique and a different compilation of data.

The other probe is RSD in galaxy clustering. Let us focus on $z \sim 1$ results, i.e. the same redshift we have been focusing on so far. Contreras et al. (2013) have estimated β from the anisotropic 2-point correlation function of about 34000 galaxies in the WiggleZ survey at an effective redshft $z = 0.76$ with an error σ_β in the range $0.11 - 0.22$, depending on the model assumed for the real-space correlation function and on the minimum transverse separation considered in the analysis.

Pezzotta et al. (2017) performed an RSD analysis on the final release of the VIPERS galaxy catalog. They quoted a result in terms of $f\sigma_8$ at $z \approx 0.85$ with an error of ~ 0.11. Using the results shown in Table 2, this implies an error $\sigma_\beta \sim 0.13$.

More recently, eBOSS Collaboration et al. (2020) presented the final results of the clustering analyses of various extra-galactic objects from the completed Sloan Digital Sky Survey (SDSS). For our comparison we are interested in the RSD-only analysis of about 170000 emission line galaxies at the effective redshift $z = 0.85$ (Tamone et al. 2020). They quote a consensus result of $f\sigma_8 = 0.315 \pm 0.095$. Taking $\sigma_8(z = 0.85) = 0.522$ from Planck ΛCDM, we find that the error on $f \ \sigma_f \sim 0.18$. This is actually comparable to the error $\sigma_f \sim 0.22$ that we predict by applying the SFLM to upcoming spectroscopic samples at $z = 1$.

Next generation surveys are designed to estimate the growth rate with higher precision. Focusing again on the Euclid case, Amendola et al. (2018) provide forecasts for the growth rate from an RSD-only analysis based, however, on somewhat outdated, optimistic assumptions on the expected number of Euclid galaxies. Their Fisher analysis indicate a relative error on f of about 1% at $z = 1$ for a flat ΛCDM cosmology (see Table 4 of their paper). More recent forecasts based on updated predictions on Euclid galaxy density has been provided by the Euclid Collaboration et al. (2019). They, however, do not consider an RSD-only analysis. Instead, they studied the case of a full shape clustering analysis that include both RSD and BAO with no additional information from CMB, low redshift surveys and weak lensing. They do not provide error on f explicitly, but on the mass density parameter Ω_m and on the parameters of the dark energy equation of state. From Table 16 in their paper, we conclude that the errors depend to a large extend on the assumed background cosmology. The relative error on f from the combined RSD+BAO range from 5% for the standard flat ΛCDM to 21% for non-flat ΛCDM; smaller than the SFLM case but very sensitive to the cosmological background model.

7. CONCLUSIONS

Motivated by the advent of large spectroscopic surveys designed to target line-emitting galaxies we have investigated the connection between the star formation rate and the underlying mass density using a suite of publicly available mock catalogs in which galaxy properties, including SFR and stellar masses, are predicted using different semi-analytic recipes for galaxy formation and evolution. The main results of our analysis can be summarized as follows:

- There are certain general properties which are qualitatively common to all mocks examined in this work: the validity of scale-independent linear bias on scales larger than $\sim 20\ \mathrm{h}^{-1}\,\mathrm{Mpc}$, insensitivity of the bias factor to the SFR for star forming galaxies with SFR larger than $\sim 3\ \mathrm{M}_\odot\,\mathrm{yr}^{-1}$, and the trend of large stellar masses and quiescent galaxies in denser environment. This is in agreement with previous findings in the literature (e.g. Angulo et al. 2014).

- Despite the above and the fact that the galaxy formation recipes incorporate the same physical processes, the corresponding mocks also exhibit distinct features that can be tested in next-generation surveys. In general, an important discriminator among models is the extent to which the large scale environment affects intrinsic relations between galaxy properties. The PDFs of the SFR and stellar mass, their redshift evolution and their variation with environment depend on the SAM recipe, especially for objects characterized by intense star formation activity and/or large stellar masses. The linear bias parameter versus SFR is model-dependent, especially at low redshifts. In particular the Galacticus model predicts, unlike all the others, a decreasing SFR as a function of the stellar mass; and for this reason should be the easiest to test through observations.

- We have shown that the SFLM is a viable method to infer the growth rate of density fluctuations. Firstly, environmental effects do not bias the β estimate obtained from the SFLM. This point has already been made before (Feix et al. 2014, 2015). Here we have demonstrated it explicitly using mock catalogs for the specific case of star forming galaxies, implying that the SFLM can be safely applied to future surveys targeting emission line galaxies. Environmental effect do contribute to random errors, though. Secondly, a point in favor of the SFLM is that these errors are small compared to shot noise and stochasticity. The former dominates the total error budget for the galaxy density expect for the Euclid survey at $z \simeq 1$. Thirdly, the uncertainties in the β estimate from the SFLM are comparable to those from RSD analyses of existing datasets at $z \sim 1$. Moreover, the SFR/luminosity shift on which the SFLM method relies upon, is rather insensitive to the parameters of the cosmological background. For example, a reasonable deviations from the Planck parameters represented by a flat Λ model with $\Omega_m = 0.2$ changes the effect by about 6% at $z = 1$. As a re-

sult, unlike most of the RSD analyses, the SFLM is rather insensitive to the assumed background cosmology and the underlying power spectrum. The SFLM constraints on the growth rate are similar across the very different SAMs considered, thus we conclude that our results are robust and model independent. For all these reasons we believe that the SFLM is an effective method to infer the growth rate.

- The SFLM method relies on SFR/luminosity shift induced by peculiar velocities V. There are two competing effects that contribute to this shift: 1) relativistic beaming, reducing the amount of light emitted by a source with positive V; this effect is independent of redshift. 2) the familiar term which at low redshift results from taking the distance as cz/H_0; this term is redshift-dependent and increases the observed luminosity compared to the true one. For the Planck cosmological parameters, the two effects cancel out at $z \approx 1.6$ while the first one becomes dominant at higher redshifts.

REFERENCES

Abate, A., & Feldman, H. A. 2012, MNRAS, 419, 3482, doi: 10.1111/j.1365-2966.2011.19988.x

Akeson, R., Armus, L., Bachelet, E., et al. 2019, arXiv e-prints, arXiv:1902.05569. https://arxiv.org/abs/1902.05569

Amendola, L., Appleby, S., Avgoustidis, A., et al. 2018, Living Reviews in Relativity, 21, 2, doi: 10.1007/s41114-017-0010-3

Angulo, R. E., Springel, V., White, S. D. M., et al. 2012, MNRAS, 426, 2046, doi: 10.1111/j.1365-2966.2012.21830.x

Angulo, R. E., White, S. D. M., Springel, V., & Henriques, B. 2014, MNRAS, 442, 2131, doi: 10.1093/mnras/stu905

Bardeen, J. M., Bond, J. R., Kaiser, N., & Szalay, A. S. 1986, ApJ, 304, 15, doi: 10.1086/164143

Bartelmann, M., & Schneider, P. 2001, Phys.Rep, 340, 291, doi: 10.1016/S0370-1573(00)00082-X

Baugh, C. M., Gonzalez-Perez, V., Lagos, C. d. P., et al. 2019, MNRAS, 483, 4922, doi: 10.1093/mnras/sty3427

Behroozi, P., Wechsler, R. H., Hearin, A. P., & Conroy, C. 2019, MNRAS, 488, 3143, doi: 10.1093/mnras/stz1182

Benson, A. J. 2012, New Astronomy, 17, 175, doi: 10.1016/j.newast.2011.07.004

Benson, A. J., Cole, S., Frenk, C. S., Baugh, C. M., & Lacey, C. G. 2000, MNRAS, 311, 793, doi: 10.1046/j.1365-8711.2000.03101.x

Bernardi, M., Sheth, R. K., Nichol, R. C., Schneider, D. P., & Brinkmann, J. 2005, ApJ, 129, 61, doi: 10.1086/426336

Binney, J. 1977, ApJ, 215, 483, doi: 10.1086/155378

Blanton, M. R., & Moustakas, J. 2009, ARA&A, 47, 159, doi: 10.1146/annurev-astro-082708-101734

Bonvin, C., Durrer, R., Gasparini, M. A., et al. 2005, PhRvD, 73, 023523, doi: 10.1103/PhysRevD.73.023523

Branchini, E., Davis, M., & Nusser, A. 2012, MNRAS, 424, 472, doi: 10.1111/j.1365-2966.2012.21210.x

Comparat, J., Prada, F., Yepes, G., & Klypin, A. 2017, MNRAS, 469, 4157, doi: 10.1093/mnras/stx1183

Contreras, C., Blake, C., Poole, G. B., et al. 2013, MNRAS, 430, 924, doi: 10.1093/mnras/sts608

Cora, S. A., Vega-Martínez, C. A., Hough, T., et al. 2018, MNRAS, 479, 2, doi: 10.1093/mnras/sty1131

Croton, D. J., Stevens, A. R. H., Tonini, C., et al. 2016, The Astrophysical Journal Supplement Series, 222, 22, doi: 10.3847/0067-0049/222/2/22

Davis, M., Nusser, A., Masters, K., et al. 2011a, MNRAS, 413, 2906, doi: 10.1111/j.1365-2966.2011.18362.x

Davis, M., Nusser, A., Masters, K. L., et al. 2011b, MNRAS, 413, 2906, doi: 10.1111/j.1365-2966.2011.18362.x

Davis, M., Nusser, A., & Willick, J. 1996, ApJ, 473, 22, doi: 10.1086/178124

Dekel, A., & Lahav, O. 1999, ApJ, 520, 24, doi: 10.1086/307428

Dekel, A., & Silk, J. 1986, ApJ, 303, 39, doi: 10.1086/164050

DESI Collaboration, Aghamousa, A., Aguilar, J., et al. 2016, ArXiv e-prints, 1611.00036. https://arxiv.org/abs/1611.00036

Disney, M. J., Romano, J. D., Garcia-Appadoo, D. A., et al. 2008, Nature, 455, 1082, doi: 10.1038/nature07366

Dolag, K., Komatsu, E., & Sunyaev, R. 2016, MNRAS, 463, 1797, doi: 10.1093/mnras/stw2035

Domínguez Sánchez, H., Mignoli, M., Pozzi, F., et al. 2012, MNRAS, 426, 330, doi: 10.1111/j.1365-2966.2012.21710.x

Dubois, Y., Peirani, S., Pichon, C., et al. 2016, MNRAS, 463, 3948, doi: 10.1093/mnras/stw2265

eBOSS Collaboration, Alam, S., Aubert, M., et al. 2020, arXiv e-prints, arXiv:2007.08991. https://arxiv.org/abs/2007.08991

Eisenstein, D. J., Seo, H.-J., Sirko, E., & Spergel, D. N. 2007, ApJ, 664, 675, doi: 10.1086/518712

Euclid Collaboration, Blanchard, A., Camera, S., et al. 2019, ArXiv e-prints, 1910.09273. https://arxiv.org/abs/1910.09273

Feix, M., Branchini, E., & Nusser, A. 2017, MNRAS, 467, 468. https://arxiv.org/abs/1612.07809

Feix, M., Nusser, A., & Branchini, E. 2014, JCAP, 09, 19, doi: 10.1088/1475-7516/2014/09/019

—. 2015, PRL, 115, 011301, doi: 10.1103/PhysRevLett.115.011301

Gao, L., & White, S. D. M. 2007, MNRAS, 377, L5, doi: 10.1111/j.1745-3933.2007.00292.x

Gene, S., Vogelsberger, M., Springel, V., et al. 2014, MNRAS, 445, 175, doi: 10.1093/mnras/stu1654

Gottlober, S., Klypin, A., & Kravtsov, A. V. 2001, ApJ, 546, 223, doi: 10.1086/318248

Gruppioni, C., Calura, F., Pozzi, F., et al. 2015, MNRAS, 451, 3419, doi: 10.1093/mnras/stv1204

Guo, Q., White, S., Boylan-Kolchin, M., et al. 2011, MNRAS, 413, 101, doi: 10.1111/j.1365-2966.2010.18114.x

Hahn, C., Blanton, M. R., Moustakas, J., et al. 2015, ApJ, 806, 162, doi: 10.1088/0004-637X/806/2/162

Hoyle, F., Rojas, R. R., Vogeley, M. S., & Brinkmann, J. 2005, ApJ, 620, 618, doi: 10.1086/427176

Huchra, J., Macri, L., Masters, K., et al. 2012, ApJS, 199, 26, doi: 10.1088/0067-0049/199/2/26

Hui, L., & Greene, P. 2006, \prd, 73, 123526, doi: 10.1103/PhysRevD.73.123526

Jing, Y. P. 2005, The Astrophysical Journal, 620, 559, doi: 10.1086/427087

Kaiser, N. 1987, MNRAS, 227, 1

Kauffmann, G., Colberg, J. M., Diaferio, A., & White, S. D. 1999, MNRAS, 303, 188, doi: 10.1046/j.1365-8711.1999.02202.x

Kauffmann, G., Nusser, A., & Steinmetz, M. 1997, MNRAS, 286, 795

Kauffmann, G., White, S. D. M., & Guiderdoni, B. 1993, MNRAS, 264, 201, doi: 10.1093/mnras/264.1.201

Keselman, A., & Nusser, A. 2016, MNRAS, 467, 1915, doi: 10.1093/mnras/stx152

Khandai, N., Di Matteo, T., Croft, R., et al. 2015, MNRAS, 450, 1349, doi: 10.1093/mnras/stv627

Knebe, A., Stoppacher, D., Prada, F., et al. 2018, MNRAS, 474, 5206, doi: 10.1093/mnras/stx2662

Krumholz, M. R., McKee, C. F., & Tumlinson, J. 2009, ApJ, 699, 850, doi: 10.1088/0004-637X/699/1/850

Lacey, C., Guiderdoni, B., Rocca-Volmerange, B., & Silk, J. 1993, ApJ, 402, 15, doi: 10.1086/172109

Larson, R. B. 1974, MNRAS, 169, 229, doi: 10.1093/mnras/169.2.229

Linder, E. V. 2005, Physical Review D, 72, 043529, doi: 10.1103/PhysRevD.72.043529

Mo, H., Yang, X., van den Bosch, F., & Jing, Y. 2004, MNRAS, 349, 205, doi: 10.1111/j.1365-2966.2004.07485.x

Moustakas, J., Coil, A. L., Aird, J., et al. 2013, ApJ, 767, 50, doi: 10.1088/0004-637X/767/1/50

Nair, P. B., van den Bergh, S., & Abraham, R. G. 2010, ApJ, 715, 606, doi: 10.1088/0004-637X/715/1/606

Nusser, A., & Branchini, E. 2000, MNRAS, 313, 587, doi: 10.1046/j.1365-8711.2000.03261.x

Nusser, A., Branchini, E., & Davis, M. 2011, \apj, 735, doi: 10.1088/0004-637X/735/2/77

Nusser, A., Branchini, E., & Davis, M. 2012, ApJ, 744, 193, doi: 10.1088/0004-637X/744/2/193

Nusser, A., Branchini, E., & Feix, M. 2013, Journal of Cosmology and Astroparticle Physics, 2013, 018

Nusser, A., & Davis, M. 1994, \apjl, 421, L1, doi: 10.1086/187172

—. 1995, MNRAS, 276, 1391

Padmanabhan, N., Xu, X., Eisenstein, D. J., et al. 2012, MNRAS, 427, 2132, doi: 10.1111/j.1365-2966.2012.21888.x

Park, C., Choi, Y., Vogeley, M. S., Gott III, J. R., & Blanton, M. R. 2007, ApJ, 658, 898, doi: 10.1086/511059

Peebles, P. J. E. 1980, The large-scale structure of the universe (Princeton University Press, NJ). http://adsabs.harvard.edu/abs/1980lssu.book.....P

Peebles, P. J. E. 1989, ApJL, 344, L53, doi: 10.1086/185529

Pezzotta, A., de la Torre, S., Bel, J., et al. 2017, A&A, 604, A33, doi: 10.1051/0004-6361/201630295

Pike, R., & Hudson, M. 2005, \apj, 635, 11, doi: 10.1086/497359

Pozzetti, L., Hirata, C. M., Geach, J. E., et al. 2016, A\&A, 590, A3, doi: 10.1051/0004-6361/201527081

Rees, M. J., & Ostriker, J. P. 1977, MNRAS, 179, 541, doi: 10.1093/mnras/179.4.541

Sachs, R., & Wolfe, A. 1967, ApJ, 147, 73, doi: 10.1086/148982

Sargent, W. L. W., & Turner, E. L. 1977, ApJL, 212, L3, doi: 10.1086/182362

Sarpa, E., Schimd, C., Branchini, E., & Matarrese, S. 2019, MNRAS, 484, 3818, doi: 10.1093/mnras/stz278

Schaye, J., Crain, R. A., Bower, R. G., et al. 2015, Monthly Notices of the Royal Astronomical Society, 446, 521, doi: 10.1093/mnras/stu2058

Sheth, R. K., & Tormen, G. 2002, MNRAS, 329, 61, doi: 10.1046/j.1365-8711.2002.04950.x

Silk, J. 1977, ApJ, 211, 638, doi: 10.1086/154972

Silk, J., & Rees, M. J. 1998, A&A, 331, L1

Somerville, R. S., & Primack, J. R. 1999, MNRAS, 310, 1087, doi: 10.1046/j.1365-8711.1999.03032.x

Springel, V., White, S. D. M., Jenkins, A., et al. 2005, Nature, 435, 629, doi: 10.1038/nature03597

Springel, V., Pakmor, R., Pillepich, A., et al. 2018, MNRAS, 475, 676, doi: 10.1093/mnras/stx3304

Strauss, M. A., Yahil, A., Davis, M., Huchra, J. P., & Fisher, K. 1992, ApJ, 397, 395, doi: 10.1086/171796

Tammann, G., Yahil, A., & Sandage, A. 1979, ApJ, 234, 775, doi: 10.1086/157556

Tamone, A., Raichoor, A., Zhao, C., et al. 2020, arXiv e-prints, arXiv:2007.09009. https://arxiv.org/abs/2007.09009

Tegmark, M. Peebles, P. 1998, ApJL, 500

Tempel, E., Saar, E., Liivamägi, L. J., et al. 2011, A&A, 529, A53, doi: 10.1051/0004-6361/201016196

White, S. D. M., & Frenk, C. S. 1991, ApJ, 379, 52, doi: 10.1086/170483

White, S. D. M., & Rees, M. J. 1978, MNRAS, 183, 341, doi: 10.1093/mnras/183.3.341

Xu, X., Zehavi, I., & Contreras, S. 2020, arXiv e-prints, 2007.05545. https://arxiv.org/abs/2007.05545

APPENDIX

A. SHOT NOISE

The variance of the shot noise in a TH smoothed galaxy density field δ_{gal} is

$$\sigma_{\text{SN}}^2 = \frac{1}{\bar{n} V_{\text{s}}} \tag{A1}$$

where $V_{\text{s}} = 4\pi R_{\text{s}}^3/3$. For the SAG mocks with the Euclid cut, $\bar{n} = 3.29 \times 10^{-3} [\text{ h}^{-1}\,\text{Mpc}]^{-3}$ giving $\sigma_{\text{SN}}^2 = 9 \times 10^{-3}$ and 7.2×10^{-5} for $R_{\text{s}} = 20$ and $100 \text{ h}^{-1}\,\text{Mpc}$, respectively.

The shot noise in the velocity can be derived as follows (c.f. Strauss et al. 1992) For simplicity, we choose to calculate the shot noise variance for the velocity recovered at the origin, $\mathbf{r} = 0$. By homogeneity, the result will be valid at any other point. The linear theory relation gives

$$\mathbf{v}(0) = -\frac{aH\beta}{4\pi\bar{n}} \sum_{r_i > R_{\text{s}}} \frac{\mathbf{r}_i}{r_i^3} - \frac{aHf}{4\pi\bar{n}} \sum_{r_i \leq R_{\text{s}}} \frac{4\pi}{3V_{\text{s}}} \mathbf{r}_i \; . \tag{A2}$$

where in the TH smoothing, each galaxy is represented as a sphere of radius R_{s}. To estimate the shot noise in this quantity, we consider boot-strap realizations in which each galaxy is replaced by N_i particles where N_i is a random integer drawn from a Poisson distribution with a mean of unity. The difference between the velocity reconstructed from one of these realizations and $\mathbf{v}(0)$ is

$$\delta\mathbf{v} = -\frac{aH\beta}{4\pi\bar{n}} \left[\sum_{r_i > R_{\text{s}}} \frac{(N_i - 1)\mathbf{r}_i}{r_i^3} + \frac{1}{R_{\text{s}}^3} \sum_{r_i \leq R_{\text{s}}} (N_i - 1)\mathbf{r}_i \right] \; , \tag{A3}$$

leading to a 1D variance

$$\sigma_{V,\text{SN}}^2 = \langle \frac{|\delta\mathbf{v}|^2}{3} \rangle = \frac{1}{3} \left(\frac{aH\beta}{4\pi\bar{n}} \right)^2 \left[\sum_{r_i > R_{\text{s}}} \frac{1}{r_i^4} + \frac{1}{R_{\text{s}}^6} \sum_{r_i \leq R_{\text{s}}} r_i^2 \right] \; . \tag{A4}$$

Transforming the summation into a volume integral using $\sum_i \rightarrow 4\pi\bar{n} \int r^2 \mathrm{d}r$ yields

$$\sigma_{V,\text{SN}}^2 = \frac{(aH\beta)^2}{10\pi\bar{n} R_{\text{s}}} \; . \tag{A5}$$

B. REGRESSIONS

The aim here is to clarify the difference between various regressions. We seek a parameter (slope) p which renders a minimum in the expression

$$\tilde{\chi}^2 = \sum_i (y_i - px_i)^2 \; , \tag{B6}$$

where x and y, respectively, have vanishing mean values. This yields the regression slope of y_i on x_i as

$$p = \frac{\sum x_i y_i}{\sum x_i^2} \; , \tag{B7}$$

with a 1σ uncertainty

$$\sigma_p^2 = \frac{\sum (y_i - px_i)^2}{\sum x_i^2} \; . \tag{B8}$$

This implies the slope of the regression of x on y is

$$q = \frac{\sigma_x^2}{\sigma_y^2} p \; . \tag{B9}$$

I. Statistically unbiased estimate of b via density-density regressions: Let $x = \delta^s$ the mass density contrast (smoothed or otherwise) and $y = \delta_{\text{gal}}^s$ to be the smoothed number density contrast of galaxies. In this case, the regression of y on x yields

$$p = \frac{\langle \delta^s \delta_{\text{gal}}^s \rangle}{\sigma_s^2} = b \; . \tag{B10}$$

where in the last line we have assumed linear biasing $\delta^s_{gal} = \delta^s + \epsilon^s$ and that the smoothed random noise term ϵ^s satisfied $\langle \epsilon^s \delta^s \rangle$. This regression yields a statistically unbiased estimate for b.

Now, take $x = \delta^s$ and $y = \delta^s_{gal}$. This is the inverse regression to the above and it gives.

$$p = \frac{\langle \delta^s \delta^s_{gal} \rangle}{\sigma^2_{s,gal}} = b \frac{\sigma^2_s}{\sigma^2_{s,gal}} = \frac{b}{1 + \sigma^2_{\epsilon^s}/\sigma^2_s} \ , \tag{B11}$$

which equals b only in the limit of vanishing σ_{ϵ^s}.

II. Let $x = \delta$ be the un-smoothed the mass density contrast and, as before, $y = \delta^s_{gal}$. The regression of y on x yields

$$p = \frac{\langle \delta \delta^s_{gal} \rangle}{\langle \delta^2 \rangle} = b \frac{\langle \delta \delta^s \rangle}{\langle \delta^2 \rangle} \ . \tag{B12}$$

Note that for a sharp k-cutoff smoothing $\langle \delta \delta^s \rangle = \langle (\delta^s)^2 \rangle$ since $\delta - \delta^s$ are composed of Fourier modes that are entirely independent from δ^s.

III. Consider the regression of $y = \delta$ on $x = \delta^s_{gal}$. Then the slope of this regression is

$$q = \frac{\langle \delta \delta^s_{gal} \rangle}{\langle (\delta^s_{gal})^2 \rangle} = b^{-1} \frac{\langle \delta \delta^s \rangle}{\langle (\delta^s)^2 \rangle + \langle (\epsilon^s)^2 \rangle / b^2} \ . \tag{B13}$$

Only for $\epsilon^s = 0$ and a sharp k-cutoff smoothing, this regression yields $1/b$.

IV. The form of the SFLM is basically a regression of true on predicted velocities. We identify x with the radial peculiar velocities, V_{rec}, predicted from the distribution of galaxies with $\beta = f$. We write

$$x = V_{rec} = V^s_{gal} + \epsilon_V \ , \tag{B14}$$

where we take the predicted velocity V_{rec} as obtained from the smoothed galaxy distribution using linear theory using the true value of β. Further, we have assumed that the smoothing is on sufficiently large scales (cf. Fig. 12) so that V_{rec} differs from the true smoothed velocities V^s_{gal} only due to shot noise and scatter in the biasing relation as represented by the term ϵ_V

As for y we take

$$y = V_{gal} + \epsilon_{SFR} \ , \tag{B15}$$

where ϵ_{SFR} represented the scatter due to the spread of the SFR. In this case, the slope is

$$p = \frac{\langle V_{gal} V^s_{gal} \rangle}{\langle (V^s_{gal})^2 \rangle + \langle (\epsilon_V)^2 \rangle} \ . \tag{B16}$$

Therefore, only if $\epsilon_V = 0$. i.e. no scatter and if V_{rec} is obtained with k-cutoff smoothing (or without any smoothing), we find the $p = 1/b$. In the application to real catalogs k-cutoff smoothing is unrealistic and it is impossible to recover the galaxy velocities without smoothing, but it is rather easy to model the expectation values of velocity products. In linear theory. Therefore, one needs to carefully calibrate the results in order to obtain a statistically estimate of β. Fortunately, this is easy to do.

C. LUMINOSITY MODULATION

Neglecting terms proportional to the gravitational potential, we have

$$\frac{z - z_t}{1 + z} \approx \frac{v}{c} \ , \tag{C17}$$

where c is the speed of light. A galaxy with measured redshift z and an observed flux, F, in units of energy (time)$^{-1}$ (area)$^{-1}$ (e.g. ergs $s^{-1}cm^{-2}$, is assigned a luminosity, L_{obs}, according

$$L_{obs} = 4\pi d^2_L(z) F \ , \tag{C18}$$

where $d_L(z)$ is the luminosity distance evaluated at redshift z.

Let us explore now how L_{obs} is related to the true intrinsic luminosity, L_{int}, of the galaxy. Let the galaxy cover an area A perpendicular to the los and let I_ν be the specific intensity of light emitted by this area in units of energy $(\text{second})^{-1}$ $(\text{area})^{-1}$ $(\text{frequency})^{-1}$ $(\text{solid angle})^{-1}$. We assume a uniform I_ν across A. We assume that the galaxy emits at a single frequency with a very narrow line such that

$$I_\nu = I\delta^D(\nu - \nu_{int}) , \tag{C19}$$

where δ^D is the Dirac-δ function. Now, $I_\nu \mathrm{d}A\mathrm{d}\Omega$ is the energy emitted per second per frequency from a small patch $\mathrm{d}A$ into a solid angle $\mathrm{d}\Omega$. Therefore, we have the

$$L_{int} = \int I_\nu \mathrm{d}\nu \mathrm{d}A\mathrm{d}\Omega = 4\pi I A . \tag{C20}$$

The observer at redshift zero measures a specific intensity $I^0_{\nu_0}$ which is related to I_ν by invariant

$$\frac{I^0_{\nu_0}}{\nu^3_0} = \frac{I_\nu}{\nu^3} , \tag{C21}$$

where

$$\nu_0 = \frac{\nu}{1+z} \tag{C22}$$

is the observed frequency. The flux measured by the observer's detector is

$$F = \Omega_A \int I^0_{\nu_0}\mathrm{d}\nu_0 \tag{C23}$$

where $\Omega_A = A/d^2_A(z_c)$ is the solid angle subtended by the area A. The angular diameter is evaluated at z_c since the area is perpendicular to the los and thus, to first order, it is unaffected by the peculiar velocity of the galaxy. Now, using the relations C19, C21 and C22, we obtain

$$\int I^0_{\nu_0}\mathrm{d}\nu_0 = I_\nu \left(\frac{\nu_0}{\nu}\right)^3 \frac{\mathrm{d}\nu_0}{\mathrm{d}\nu}\mathrm{d}\nu = \frac{I}{(1+z)^4} . \tag{C24}$$

This is Tolman's surface brightness law. Therefore,

$$F = \frac{IA}{d^2_A(z_c)(1+z)^4} = \frac{L_{int}}{4\pi d^2_A(z_c)(1+z)^4} \tag{C25}$$

Using Eq. C18 and remembering that $d_L(z) = (1+z)^2 d_A(z)$ we find

$$L_{obs} = \left[\frac{d_A(z)}{d_A(z_c)}\right]^2 L_{int} . \tag{C26}$$

We have arrived at a peculiarity result that the modulation of the luminosity is actually via the angular diameter distance rather that the luminosity distance.

Let us expand the distance ratio to first order in V. We start with

$$d_A = \frac{d_C}{1+z} \tag{C27}$$

where

$$d_C = c \int_0^z \frac{\mathrm{d}z}{H(z)} , \tag{C28}$$

is the comoving distance.

First order Taylor expansion of $d_A(z)$ in the vicinity of $z \approx z_c$ is

$$d_A(z) = d_A(z_c) - \frac{z - z_c}{1+z_c}\frac{d_C(z_c)}{1+z_c} + \frac{z - z_c}{1+z_c}\frac{\mathrm{d}d_C(z_c)}{\mathrm{d}z} \tag{C29}$$

$$= d_A(z_c)\left[1 - \frac{V}{c} + \frac{V}{H(z_c)d_A(z_c)}\right] . \tag{C30}$$

The last line is consistent with previous findings in the literature (Bonvin et al. 2005; Hui & Greene 2006). In the square brackets, The V/c reflects relativistic beaming which goes in the opposite direction of the second term arising from associating the distance with redshift. To first order, we can replace z_c by z in the term in brackets. Therefore, given the velocities (via a model) L_{int} can be estimated as

$$L_{int}^e = L_{obs} \left[1 + \frac{2V}{c} - \frac{2V}{H(z)d_A(z)} \right] . \tag{C31}$$

We can easily include all other relativistic effected related to the gravitational potential. Over the scales considered here, gravitational lensing is dominant. The modification to the equations Eq. C25 and Eq. C26 due to lensing is simple: $d_A(z)$ remains the same and given by the expressions Eq. C27 & Eq. C28, while

$$d_A(z_c) \to \tilde{d}_A(z_c, \kappa) = d_A(z_c)(1 - \kappa) , \tag{C32}$$

where κ is the convergence given in terms of a los integral over he density contrast. This reflects the fact that objects appear to occupy larger solid angles for positive κ. Therefore,

$$d_A(z) = d_A(z_c) \left[1 - \frac{V}{c} + \frac{V}{H(z_c)d_A(z_c)} - \kappa \right] . \tag{C33}$$

Let us consider a small patch of the survey at a given redshift and where κ and V can be assumed constant. Let F_l be the limiting flux of the survey. The minimum threshold observed luminosity for this patch is

$$L_{obs,l} = 4\pi(1 + z)^2 d_A^2(z) F_l . \tag{C34}$$

The threshold intrinsic luminosity is (cf. Eq. C26)

$$L_{int,l} = 4\pi(1 + z)^2 \tilde{d}_A^2(z_c) F_l . \tag{C35}$$

Thus the actual threshold intrinsic luminosity of galaxies in a given range of observed redshift z in the patch will depend on κ and the los velocity, V. The number density will therefore chance and this will affect the variance of $\log L_{int}^e$ estimated from L_{obs} using Eq. C31, in addition to the modulation of L_{int}^e by V. In the tests provided in the paper, we do not include the effect related to the change in the threshold luminosity.

In the above, it may seem that there is a degeneracy between κ and the velocity corrections. The convergence κ is a los integrated quantity and can actually be estimated from the distribution of galaxies assuming a biasing relation.

The observer's Since we are considering line luminosity, there are no issues related to k-correction present in the case of measuring magnitudes in a given band.

D. GRAVITATIONAL LENSING

Gravitational lensing by foreground mass distribution modifies the observed luminosity/SFR of a galaxy by a multiplicative factor $1 + 2\kappa$ where (Bartelmann & Schneider 2001)

$$\kappa = \frac{3H_0^2 \Omega_m}{2c^2} \int_0^r dr' g(r', r) \delta(r\hat{\mathbf{r}}) , \tag{D36}$$

where the galaxy is at $\mathbf{r}$ and $g(r', r) = (r' - r'^2/r)/a(r')$. Following the derivation in Nusser et al. (2013), we obtain

$$C_l = \frac{2}{\pi} \left(\frac{3H_0^2 \Omega_m}{2c^2} \right)^2 \int dk k^2 P(k) | \int_0^r dr' g(r', r) j_l(kr')|^2 . \tag{D37}$$

Working with the Limber's approximation for the spherical Bessel functions $j_l(kr) \sim \sqrt{\frac{\pi}{l+1/2}} \delta^D(l + 1/2 - kr)$, the relation becomes

$$C_l = (2l + 1) \left(\frac{3H_0^2 \Omega_m}{2c^2} \right)^2 \int_{k=(l+1/2)/r}^\infty dk P(k) \left(1 - \frac{2l + 1}{2kr} \right)^2 \tag{D38}$$

The variance of κ is then

$$\sigma_\kappa^2 = \sum_{l=0}^\infty W_l^2 C_l \approx \sum_{l=0}^{l_{max}} \frac{2l + 1}{4\pi} C_l , \tag{D39}$$

where W_l represents averaging over a solid angle $\pi\theta_s^2$ where $\theta_s = R_s/r$. In the second part of this equation, the effect of this window function is approximated in terms the sharp l-cutoff at $l_{lmax} = 2r/R_s$. For $R_s = 20$ and $100 \, h^{-1}$ Mpc the expression yields, respectively, $\sigma_\kappa \approx 2 \times 10^{-3}$ and 3×10^{-4}. This translates into log SFR shifts of $\log(1 + 2\sigma_\kappa) \approx 1.6 \times 10^{-3}$ and 2.5×10^{-4} for the smaller and larger R_s respectively.